

## KINEMATICS OF THE STELLAR HALO AND THE MASS DISTRIBUTION OF THE MILKY WAY USING BHB STARS

PRAJWAL R. KAFLE<sup>1</sup>, SANJIB SHARMA, GERAINT F. LEWIS & JOSS BLAND-HAWTHORN

Sydney Institute for Astronomy, School of Physics, A28, The University of Sydney, NSW 2006, Australia

Draft version June 29, 2018

### ABSTRACT

Here we present a kinematic study of the Galactic halo out to a radius of  $\sim 60$  kpc, using 4664 blue horizontal branch (BHB) stars selected from the SDSS/SEGUE survey, to determine key dynamical properties. Using a maximum likelihood analysis, we determine the velocity dispersion profiles in spherical coordinates ( $\sigma_r$ ,  $\sigma_\theta$ ,  $\sigma_\phi$ ) and the anisotropy profile ( $\beta$ ). The radial velocity dispersion profile ( $\sigma_r$ ) is measured out to a galactocentric radius of  $r \sim 60$  kpc, but due to the lack of proper-motion information,  $\sigma_\theta$ ,  $\sigma_\phi$  and  $\beta$  could only be derived directly out to  $r \sim 25$  kpc. From a starting value of  $\beta \approx 0.5$  in the inner parts ( $9 < r/\text{kpc} < 12$ ), the profile falls sharply in the range  $r \approx 13 - 18$  kpc, with a minimum value of  $\beta = -1.2$  at  $r = 17$  kpc, rising sharply at larger radius. In the outer parts, in the range  $25 < r/\text{kpc} < 56$ , we predict the profile to be roughly constant with a value of  $\beta \approx 0.5$ . The newly discovered kinematic anomalies are shown *not* to arise from halo substructures. We also studied the anisotropy profile of simulated stellar halos formed purely by accretion and found that they *cannot* reproduce the sharp dip seen in the data. From the Jeans equation, we compute the stellar rotation curve ( $v_{\text{circ}}$ ) of the Galaxy out to  $r \sim 25$  kpc. The mass of the Galaxy within  $r \lesssim 25$  kpc is determined to be  $2.1 \times 10^{11} M_\odot$ , and with a 3-component fit to  $v_{\text{circ}}(r)$ , we determine the virial mass of the Milky Way dark matter halo to be  $M_{\text{vir}} = 0.9_{-0.3}^{+0.4} \times 10^{12} M_\odot$  ( $R_{\text{vir}} = 249_{-31}^{+34}$  kpc).

*Subject headings:* galaxies: individual (Milky Way)-Galaxy: halo - stars: horizontal-branch - stars: kinematics

### 1. INTRODUCTION

Understanding the formation of stellar halos gives vital insight into the formation history and the evolution of galaxies (Majewski 1993; Freeman & Bland-Hawthorn 2002; Helmi 2008). Under the currently favored  $\Lambda$ CDM model of galaxy formation, the stellar halos are thought to have been built up, at least in part, by accretion of satellite galaxies (White & Rees 1978; Searle & Zinn 1978; Helmi & White 1999). Discoveries of structures like the Sagittarius dwarf galaxy (Ibata et al. 1994, 1995; Majewski et al. 2003; Belokurov et al. 2006), the Virgo over-density (Jurić et al. 2008), the Triangulum-Andromeda structure (Rocha-Pinto et al. 2004; Majewski et al. 2004; Martin et al. 2007) and the low-latitude Monoceros ring (Newberg et al. 2002) lend further support to the idea of the stellar halo being formed by accretion. Other than accretion, a part of the stellar halo could also be formed by in-situ stars. Recent hydro-dynamical simulations (Abadi et al. 2006; Zolotov et al. 2009; Font et al. 2011; McCarthy et al. 2012) of galaxy formation suggest that in the inner regions the stellar halo might be dominated by in-situ stars, whose kinematic properties are distinct from the accreted stars.

Observational evidences of multi-component halo have been found in dynamical studies of SDSS calibration stars (Carollo et al. 2007, 2010; Beers et al. 2012), in rotational behavior in metallicity bins (Deason et al. 2011a), in kinematics of Galactic anti-center and North Galactic Pole population (Kinman et al. 2007), in chemical properties (de Jong et al. 2010), and also in age difference between in-situ and accreted halo (Kalirai 2012). There also exists a counter-claim by Schönrich et al. (2011), who demonstrate that the evidence of retrograde signal in the outer halo in Carollo et al. (2010) sample is weak and is because of a manifestation of incorrect distance estimates. Investigating, whether any signal of

multi-component halo could also be seen in the dispersions of the velocity of the halo population is important. Ultimately, studying the velocity dispersion profiles of the halos and comparing them with simulations might help to constrain the model of galaxy formation.

Lack of proper motions and the slightly off centered position of the Sun with respect to the galactic center poses a unique challenge in studying the kinematics of the stellar halo. At distances much larger than  $R_\odot$ , line of sight velocity is same as radial velocity with respect to the galactic center. Hence the  $\sigma_r$  profile is easy to compute at large distances and this has been well studied; Battaglia et al. (2005) studied the line-of-sight velocity dispersion ( $\sigma_{\text{los}}$ ) of a mixture of 240 halo objects and found that  $\sigma_{\text{los}}$  decreases monotonically beyond  $r \sim 30$  kpc. In the outer most halo at  $r \sim 100$  kpc Battaglia et al. (2005) and recently, Deason et al. (2012b) both see a significant drop in  $\sigma_{\text{los}}$  value to  $\sim 50 \text{ km s}^{-1}$ .

Conversely, De Propris et al. (2010) studied 666 BHB stars from the 2QZ Redshift Survey and found the velocity dispersion profile increases at large distances. But using 910 distant halo A-type stars, Brown et al. (2010) found that there is a mean decline of  $-0.38 \pm 0.12 \text{ km s}^{-1} \text{ kpc}^{-1}$  in  $\sigma_r$  over  $15 < r/\text{kpc} < 75$ . More recently, Xue et al. (2008) used 2401 BHB halo stars within 60 kpc and measured a slower decline in  $\sigma_{\text{los}}$  compared to earlier studies. At small  $r$  it has been difficult to derive the  $\sigma_r$  profile, and the only attempt to measure the  $\sigma_r$  in inner-halo was undertaken by Sommer-Larsen et al. (1997). They find a sharp fall in  $\sigma_r$  from  $\sim 140 \text{ km s}^{-1}$  to  $\sim 100 \text{ km s}^{-1}$  at  $r \approx 12$  kpc although they assume the circular velocity to be constant.

In a solar neighborhood one can get useful proper motions and with this all the three velocity dispersions ( $\sigma_r$ ,  $\sigma_\theta$ ,  $\sigma_\phi$ ) can be measured. Smith et al. (2009a) used the full phase space information of  $\sim 1700$  halo subdwarfs from the solar neighborhood ( $< 5$  kpc) and determined the velocity dispersions to be  $(\sigma_r, \sigma_\theta, \sigma_\phi) = (143 \pm 2, 82 \pm 2, 77 \pm 2) \text{ km s}^{-1}$ .

<sup>1</sup> p.kafle@physics.usyd.edu.au

Also, Bond et al. (2010) analyzed the proper motions of a large sample of main-sequence stars within the solar neighborhood ( $< 10$  kpc) and found  $\sigma_r = 141 \text{ kms}^{-1}$ ,  $\sigma_\theta = 75 \text{ kms}^{-1}$ ,  $\sigma_\phi = 85 \text{ kms}^{-1}$ . A summary of the estimated values of the velocity dispersions found in the literature is given in Table 1.

Due to the lack of reliable proper motions of the halo field stars, even the fundamental quantities like the tangential components of the velocity dispersions as well as the anisotropy ( $\beta$ ) are still badly understood beyond solar neighborhood. The situation is however not as hopeless as it might seem. At small  $r$ , using only line of sight velocity it is possible to put some constraints on these quantities using maximum likelihood techniques, where a model or a distribution function needs to be specified *a priori*. In an analysis of 1170 BHB stars ranging from  $5 \lesssim d/\text{kpc} \lesssim 96$ , where  $d$  is now the stellar distance rather than a radius, Sirko et al. (2004b) fit an ellipsoidal distribution of velocities and find that the halo is isotropic. Similarly, Deason et al. (2011a, hereafter D11) fit a constant anisotropy model (power law Distribution Function) to 3549 BHB stars constructed from the SDSS Data Release 7 (DR7) and find that the halo between  $r = 10 - 25$  kpc is tangential whereas the distant halo within  $25 < r/\text{kpc} < 50$  is radial. D11 claims for the tangential inner halo are in contrast with the result by Bond et al. (2010) who found the inner halo to be radial in the similar region ( $d \approx 10$  kpc). D11 assume the distribution function (DF) to be such that the tracer density and the potential both are power laws. Without *a priori* knowledge of the density slope their estimates will have some systematics. Additionally, the potential was also kept constant in their analysis and thus can bias the results due to the degeneracy between the potential and the anisotropy.

In their most recent work, Deason et al. (2012a, hereafter D12) allow both the potential and  $\beta$  to vary and thereby break the degeneracy, and find that the outer halo within  $16 < r/\text{kpc} < 48$  is radial with  $\beta = 0.5^{+0.1}_{-0.2}$ . Previous estimates of the velocity anisotropy ( $\beta$ ) in the solar neighborhood and the nearby halo are summarized in Table 1. All the above estimates of an anisotropy of the distant halo is done in a large radial bins. Their results might be accurate for the given radial bins and could also be the actual anisotropy of the halo provided the anisotropy remains nearly constant or monotonic through out. On the other hand, if the actual  $\beta$  of the system is not monotonic but has a more complex shape, then estimating it in the larger bin will just capture an overall property of that bin.

Theoretically there are families of the distribution function of Henon (1973) type which result in a constant anisotropic system, as well with the families of models those have their own anisotropy profiles, which include Osipkov-Merritt model (Osipkov (1979); Merritt (1985a,b)), Gerhard (1991), Cuddeford (1991), Baes & van Hese (2007) and few more with the Hernquist potential-density model in Baes & Dejonghe (2002). The question we ask is how well do these anisotropy profiles match the anisotropy of the Galaxy? More fundamentally, how well do we know the anisotropy of the halo? To this end we thus compute the beta profile with much finer spatial resolution and without any prior assumptions about density or potential.

Another use of studying the kinematics of the stellar halo is to constrain the mass and the potential of the Milky Way. Most of the methods to estimate the mass require the knowledge of the anisotropy parameter  $\beta$ . Without the unbiased estimate of the velocity anisotropy, constraining the mass of

the system via the Jeans equation could be uncertain by 73% (for  $-4.5 < \beta < 0.44$ ) as found by Watkins et al. 2010 in their estimates of mass of the Galaxy. Several other authors have also used this assumption to estimate the mass of the galaxy (Dehnen et al. 2006; Gnedin et al. 2010; Deason et al. 2012b). Precaution needs to be taken while making an arbitrary assumption about the anisotropy. It has been found that the halo stars, the satellites and the dark matter halo have different orbital properties (Abadi et al. 2006; Sales et al. 2007). Hence assuming a constant anisotropy for both field stars as well as satellites (Battaglia et al. 2005; Dehnen et al. 2006) could introduce systematic uncertainties in the mass estimate. Ideally, in order to break the degeneracy we must have a separate estimation of the radial velocity dispersion, the velocity anisotropy and underlying density of the population, as pointed out by Dehnen et al. (2006).

The orbital evolution of the Magellanic clouds (Lin & Lynden-Bell 1982; Besla et al. 2007), the local escape speed (Smith et al. 2007), the timing argument (Li & White 2008) and the study of the kinematic of the tracers population (Kochanek 1996; Xue et al. 2008; Gnedin et al. 2010; Watkins et al. 2010) are the methods undertaken in order to constrain the mass of the Galaxy. Summarizing all these attempts to constrain the mass of the Galaxy, the consensus can be found between  $0.5 - 3.5 \times 10^{12} M_\odot$ . Recently using BHB stars Xue et al. (2008) estimate the mass of the Milky Way to be  $0.91^{+0.27}_{-0.18} \times 10^{12} M_\odot$ . However, they make an assumption that the variation of ( $v_{\text{circ}}/v_{\text{los}}$ ), the ratio of the circular to the line of sight velocity, with radius is same as that in simulations. In this paper, we estimate  $v_{\text{circ}}$  as far out as possible without any assumption and then use it to estimate the dark matter halo mass.

This work focuses mainly on the study of the kinematics of the stellar halo in order to present the unbiased estimation of the velocity dispersions, anisotropy parameter and circular velocity as a function of radius to the extent data supports. We use a DF which does not require any assumption to be made *a priori* about the density profile or the potential. We then use our measurements of velocity dispersions to estimate the rotation curve of the Galaxy. The disc and bulge mass already being constrained from Sofue et al. (2009), we focus on constraining the dark matter halo mass. Using the circular velocity curve ( $v_{\text{circ}}(r)$ ) we can estimate  $\beta(r)$  out to as far as  $\sigma_r(r)$  is available. Finally, we compare our results with simulations in which the halo is formed purely by accretion.

This paper is organized as follows: in Section 2 we discuss the theoretical aspect of our analysis, the methodology adopted, and the details about the sample; in Section 3 we present our result for the velocity dispersions, confer the results between the alternative models, and investigate the contribution of the halo substructures; in Section 5 we present our estimation of the mass of the Galaxy. Results are then compared with the simulations in Section 6. In Section 7 we present our conclusion and discuss our result.

## 2. THEORY AND METHOD

We are interested in calculating the velocity dispersions ( $\sigma_r, \sigma_\theta, \sigma_\phi$ ) for the stellar halo. However, the data we have is line of sight velocities. To proceed we need to make some assumptions about the position and the velocity of the Sun with respect to the galactic center. We assume  $R_\odot = -8.5$  kpc, the velocity of the local standard of rest (LSR),  $v_{\text{LSR}}$ , is taken to be IAU adopted value =  $220 \text{ kms}^{-1}$ , and the solar motion with respect to LSR (U, V, W) $_\odot = +11.1, +12.24, +7.25$  in

**Table 1**  
Velocity Dispersions and Anisotropy Reference Table

Sample (number)	distance (kpc)	$\sigma_r, \sigma_\theta, \sigma_\phi$ (kms <sup>-1</sup> )	anisotropy ( $\beta$ )	Reference
BHB ( $\sim 700$ )	( $r \lesssim 20, r \gtrsim 45$ )	$\sigma_r = (140, 90 - 110)$	(radial(0.5), tangential(-1.3))	Sommer-Larsen et al. 1997
BHB (1170)	$5 \lesssim d \lesssim 96$	$101.4 \pm 2.8, 97.7 \pm 16.4, 107.4 \pm 16.6$	nearly isotropic	Sirko et al. 2004b
BHB (1933)	$16 < r < 48$	-	radial ( $0.5_{-0.2}^{+0.08}$ )	Deason et al. 2012a
Subdwarfs ( $\sim 1700$ )	$d < 5$	$143 \pm 2, 82 \pm 2, 77 \pm 2$	radial ( $\sim 0.69$ )	Smith et al. 2009b
MS ( $10^5$ )	$d \simeq 10$	141,75,85	radial ( $\sim 0.67$ )	Bond et al. 2010
BHB (3549)	( $10 < r < 25, 25 < r < 50$ )	-	(tangential(-0.6), radial(0.5))	Deason et al. 2011a

kms<sup>-1</sup> (Schönrich et al. 2010). Spherical and heliocentric coordinate system are expressed in terms of  $(r, \theta, \phi)$ , and  $(d, l, b)$  respectively.

### 2.1. Distribution Function

The distribution function (DF),  $f$ , is defined such that  $f(\mathbf{x}, \mathbf{v}) d^3\mathbf{x} d^3\mathbf{v}$  is the probability of finding a randomly picked star in a phase-space volume  $d^3\mathbf{x} d^3\mathbf{v}$ . In general, we consider the stellar halo as an anisotropic spherical system. The anisotropy is defined as

$$\beta = 1 - \frac{\sigma_\theta^2 + \sigma_\phi^2}{2\sigma_r^2}, \quad (1)$$

$\sigma_r, \sigma_\theta$  and  $\sigma_\phi$  being the velocity dispersions in spherical coordinates, and it describes the orbital structure of the system. The values of this parameter range from  $-\infty$  for purely circular trajectories to 1 for purely radial orbits.

Families of DFs that generate the collisionless anisotropic spherical systems with constant or varying velocity anisotropy can be found in detail in Binney & Tremaine (2008). One such distribution function with constant anisotropy is

$$f(E, L) = f(E)L^{-2\beta}. \quad (2)$$

Here  $E = \Phi(r) - (v^2/2)$  is the relative energy per unit mass and  $L$  is the modulus of the angular momentum vector per unit mass. Recently, a DF given by Equation (2) with the energy term from Evans et al. (1997):

$$f(E, L) \propto E^{(\beta(\gamma-2)/\gamma) + (\alpha/\gamma) - 3/2} L^{-2\beta}, \quad (3)$$

was used by Deason et al. (2011a) and Deason et al. (2012a) to study the rotation, anisotropy and mass of the Galactic halo. The parameters  $\alpha$  and  $\gamma$  are the logarithmic slopes of the density ( $\rho \propto r^{-\alpha}$ ) and potential ( $\Phi \propto r^{-\gamma}$ ) respectively. Hereafter, we refer to this function as D11 DF.

If one is interested in deriving the dispersion profiles, a simple distribution function that one can use is the Gaussian velocity ellipsoidal distribution function (GVE DF). The GVE DF has been used in the context of the stellar halo by Frenk & White (1980) using globular clusters as tracers and by Sirko et al. (2004b) and Smith et al. (2009b) using halo stars. A GVE DF with rotation about z-axis is given by

$$f(r, \mathbf{v}) = \frac{\rho(r)}{(2\pi)^{3/2} \sigma_r \sigma_\theta \sigma_\phi} \exp \left[ -\frac{1}{2} \left( \frac{v_r^2}{\sigma_r^2} + \frac{v_\theta^2}{\sigma_\theta^2} + \frac{(v_\phi - v_{\text{rot}})^2}{\sigma_\phi^2} \right) \right] \quad (4)$$

The DF as given by Equation (4) assumes that the velocity ellipsoid is perfectly aligned with the spherical coordinates, but in general the velocity ellipsoid can have a tilt. Using halo subdwarf stars Smith et al. (2009a) and Bond et al. (2010) have found that the tilt is small and consistent with zero. Hence, it is safe to ignore the tilt while computing velocity dispersions.

### 2.2. Parameter estimation

The proper motion information of the stars in the stellar halo beyond solar neighborhood ( $r \gtrsim 10$  kpc) is not accurate enough to properly constrain the tangential motions. Nevertheless, our position in the Galaxy still makes it possible to constrain these quantities by utilizing the tangential information carried by the line-of-sight velocities of the stars. However, for that we need to marginalize the distribution function over the unknown quantities, which in this case are the tangential components ( $v_l, v_b$ ). The expression for the marginalized DF is given by,

$$F(l, b, d, v_{\text{los}} | \sigma_r, \sigma_\theta, \sigma_\phi, v_{\text{rot}}) = \iint f dv_l dv_b. \quad (5)$$

We use maximum likelihood method to estimate the model parameters. The log-likelihood function which we maximize is given by

$$\mathcal{L}(l, b, d, v_{\text{los}} | \sigma_r, \sigma_\theta, \sigma_\phi, v_{\text{rot}}) = \sum_i^n \log F(l_i, b_i, d_i, v_{\text{los}_i}), \quad (6)$$

where  $n$  is the number of stars in the system under study. We use Markov Chain Monte-Carlo (MCMC) with the Metropolis Hasting algorithm (MHA) to obtain the posterior distribution. We quote the central values of the velocity dispersions ( $\sigma_r, \sigma_\theta, \sigma_\phi$ ) as our initial estimates and 16 and 84 percentiles as the error associated. Note, for the GVE DF the density term  $\rho(r)$  in Equation (4) is not a function of model parameters and hence it does not have any effect on the likelihood analysis.

Once the radial velocity dispersion  $\sigma_r$  and the anisotropy parameter  $\beta$  are evaluated, Jeans equation (Jeans 1915) can be used to estimate the circular velocity  $v_{\text{circ}}$  of the spherical system in equilibrium using the relation

$$v_{\text{circ}}^2(r) = -\sigma_r^2 \left[ \frac{d \ln \rho}{d \ln r} + \frac{d \ln \sigma_r^2}{d \ln r} + 2\beta \right], \quad (7)$$

where  $\rho \propto r^{-\alpha}$  is the density of the tracer population, which implies  $d \ln \rho / d \ln r = -\alpha$ . Through out the analysis we assume the density to be double power law with  $\alpha = 2.4$  ( $r \leq 27$  kpc) and  $\alpha = 4.5$  ( $r > 27$  kpc) in agreement with the recent works by Deason et al. (2011b) and Watkins et al. (2009).

For systems with constant anisotropy and a given  $v_{\text{circ}}$ , the solution to the differential equation (7) subject to the boundary condition  $\lim_{r \rightarrow \infty} \sigma_r^2 = 0$  reads

$$\sigma_r^2(r) = \frac{1}{r^{2\beta} \rho(r)} \int_r^\infty dr' r'^{2\beta} \rho(r') (d\Phi/dr') \quad (8)$$

Assuming density and anisotropy are known we can use this solution to estimate  $\sigma_r$  as a function of  $r$ .

### 2.3. DATA: BHB stars

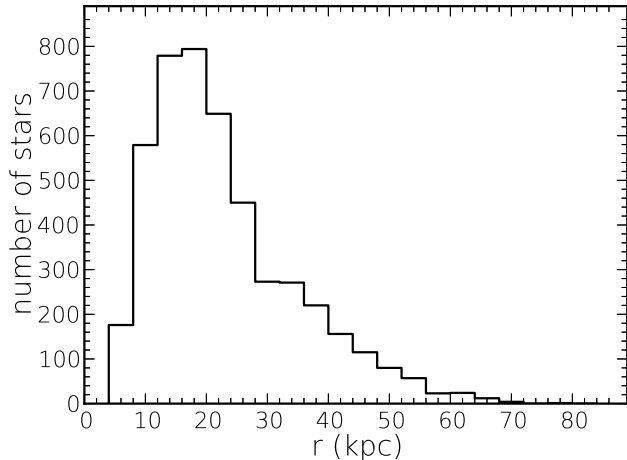


**Figure 1.** Radial distribution of BHB stars in galactocentric coordinates. The distribution has a peak at around 16 kpc. Most of the stars are found to lie in the range  $10 < r/\text{kpc} < 25$ .

Being luminous and having nearly constant magnitude BHB stars are ideal for studying the stellar halo, and this is what we use in our study. We use the BHB catalog published by X11 for our analysis. The catalog comprises of 4985 BHB stars obtained from Sloan Digital Sky Survey (SDSS) Data Release 8 (Aihara et al. 2011). The stars were selected by imposing limits on color and Balmer line profile measurements. Imposing limits on Balmer line profile measurements allow one to remove the main sequence stars and Blue Stragglers. Further details on BHB candidate selection can be found in Xue et al. (2008) and references therein. To avoid contamination from the disk stars, we restrict our analysis to stars having a distance  $|z| > 4$  kpc from the galactic mid-plane. As mentioned earlier, the way our likelihood function (Equation 5) is laid out, this cut in distance above the plane will not introduce any bias. No velocity limits have been imposed to obtain the sample and thus for the purpose of kinematic studies the population of BHB stars we select can be considered to be kinematically unbiased.

For the stars that we study the angular position is known very accurately, but the distance and radial velocity have some uncertainty associated with them. To get more accurate distances we recalibrate X11 distances using a color-magnitude relation derived for the same population from Deason et al. (2011b). The estimated dispersion in g-band magnitudes is 0.13, equivalent to a distance uncertainty of 6%. For the SEGUE (Yanny et al. 2009) radial velocity measurements, 94% of our sample have an uncertainty of less than  $8 \text{ km s}^{-1}$ .

The galactocentric radial distribution of the final BHB samples is shown in Figure 1. It can be seen that the distribution peaks at around 16 kpc. Most of the stars are found to lie in the range  $10 < r/\text{kpc} < 25$ .

### 3. VELOCITY DISPERSION PROFILE OF THE HALO

We study the kinematics of the halo in radial bins to obtain radial profile of the model parameters ( $\sigma_r, \sigma_\theta, \sigma_\phi$ ) and also  $\beta$ . Using only line-of-sight velocity information the tangential components,  $\sigma_\theta$  and  $\sigma_\phi$ , are difficult to constrain except in the very inner regions of the halo. However,  $\sigma_r$  can be well constrained both in the inner and the outer halo. This means that relatively larger number of stars ( $>1000$ ) per bin are required to estimate  $\sigma_\theta$  and  $\sigma_\phi$  as compared to  $\sigma_r$ . Given that we only have about 4000 stars this means that we cannot

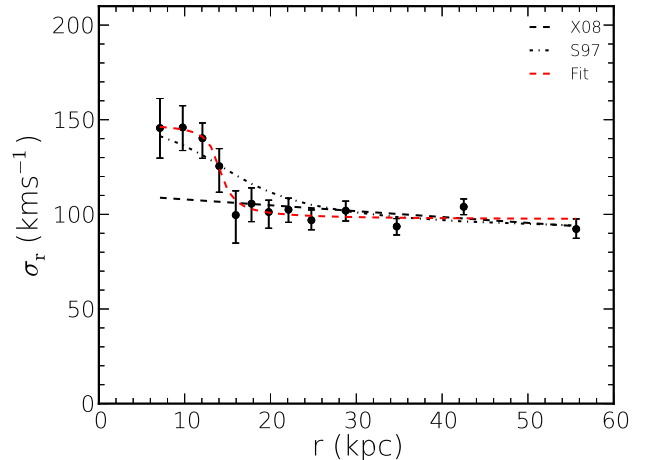


**Figure 2.** Radial velocity dispersion in radial bins. The black dashed line is the  $\sigma_{\text{los}}$  profile from Xue et al. (2008). Black dashed-dotted and red dashed lines are the Sommer-Larsen profiles given by Equation (9) for the fitting parameters taken from Sommer-Larsen et al. (1997) and from the fit to our estimated values of  $\sigma_r$  respectively.

measure the  $\sigma_\theta$  and  $\sigma_\phi$  profiles with sufficient spatial resolution. Hence, we employ two different binning schemes or estimators, one for radial velocity and the other for tangential velocity. The estimators are; the equi-populated estimator (hereafter EPE) and central moving estimator (CME). In EPE the data is binned radially with each bin containing equal number of particles and this is used for computing  $\sigma_r(r)$ . In CME a set of equi-spaced positions in  $r$  are chosen and then at each position an equal number of points either side of the chosen central value are used to estimate the desired quantity. We use the CME for computing  $\sigma_\theta(r)$  and  $\sigma_\phi(r)$ . The crucial difference between the two schemes is that while the bins are non-overlapping in the former, in the latter they can be overlapping. In EPE the spacing between the bins is directly proportional to the number of particles in each bin  $n_{\text{bin}}$ . Hence, if the desired quantity can be estimated with sufficient accuracy employing small  $n_{\text{bin}}$ , then EPE is the desired method. However, if this is not the case then it is better to use the CME method as the spatial resolution is not directly dependent on  $n_{\text{bin}}$ <sup>1</sup>.

Finally, for our data the number density of points in  $r$  is highly non-uniform, and hence it is not accurate to assume that the desired quantity has been estimated at the center of the bin. To alleviate this number density bias, for both schemes we compute the final position of the bin as the mean  $r$  of the points in the bin.

#### 3.1. Radial velocity dispersion profile ( $\sigma_r(r)$ )

Here we focus on the nature of the  $\sigma_r(r)$  profile of the halo for which we adopt the EPE method with  $n_{\text{bin}} = 400$ . As explained previously,  $\sigma_r$  can be measured out to the extent of the data ( $r \sim 60$  kpc). The values of  $\sigma_r$  obtained from the likelihood analysis are given in Figure 2 and the error bars represent the  $1\sigma$  confidence interval and are determined from the likelihood fitting.

We find that the radial velocity dispersion,  $\sigma_r$  at the Sun's position ( $R_\odot = 8.5$ ) is  $145.6 \text{ km s}^{-1}$ . However, beyond the solar neighborhood  $\sigma_r$  sharply decreases until  $r \sim 15$  kpc, after which it decreases much slowly and approaches a value

<sup>1</sup> For the effect of the bin size, see appendix A.

of around  $\sim 100 \text{ km s}^{-1}$  at 56 kpc. The error bar in  $\sigma_r$  for the inner halo population is large and is mainly because the  $v_{\text{los}}$  contains less radial velocity information as compared to outer parts. The overlaid black dashed line is the linear approximation ( $\approx 111 - 0.31r$ ) for  $\sigma_{\text{los}}$  profile from Xue et al. (2008). Additionally, other previous attempts to fit the profile for  $\sigma_r$  in the outer parts of the halo (Battaglia et al. 2005; Gnedin et al. 2010; Brown et al. 2010) also found profiles similar to Xue et al. (2008), with slightly varying slope and normalization. All these profiles are reasonable estimates of  $\sigma_r$  for the outer halo ( $d \gg R_{\odot}$ ) where the assumption  $\sigma_r \approx \sigma_{\text{los}}$  holds. In the inner halo ( $r \lesssim 15 \text{ kpc}$ ) however the approximation breaks down and  $\sigma_r$  strongly deviates from  $\sigma_{\text{los}}$ . It can be seen that the deviation of  $\sigma_r$  from  $\sigma_{\text{los}}$  increases as one approaches the center and at  $R_{\odot}$  the deviation is as high as  $\sim 40 \text{ km s}^{-1}$ .

Sommer-Larsen et al. (1997) provide a functional form for fitting the  $\sigma_r$  profiles which is given by

$$\sigma_r^2 = \sigma_0^2 + \frac{\sigma_+^2}{\pi} \left[ \frac{\pi}{2} - \tan^{-1} \left( \frac{r-r_0}{l} \right) \right]. \quad (9)$$

This has a shape which is similar to our  $\sigma_r(r)$  profile and we fit it to find  $\sigma_0 = 94.5 \text{ km s}^{-1}$ ,  $\sigma_+ = 122.3 \text{ km s}^{-1}$ ,  $r_0 = 13.2 \text{ kpc}$ , and  $l = 2.6 \text{ kpc}$ . In this function the fit parameter  $\sigma_0$  gives the asymptotic value that  $\sigma_r$  achieves in the outer halo, whereas  $(\sigma_0^2 + \sigma_+^2)^{1/2}$  gives the approximate value for  $\sigma_r$  in the inner halo. The fit parameters  $r_0$  and  $l$  determine the turn-off point and the steepness of the transition of the profile respectively. A lower value of  $l$  gives a steeper transition, this can be seen from the comparison between the Sommer-Larsen fit ( $l = 7.5 \text{ kpc}$ ) and the red line in Figure 2 which is our fit having smaller  $l$ .

### 3.2. Tangential velocity dispersion and anisotropy profiles ( $\sigma_{\theta}(r)$ , $\sigma_{\phi}(r)$ and $\beta(r)$ )

There have been few attempts to constrain the tangential velocity dispersions and most of the studies are either restricted to solar neighborhood (Smith et al. 2009b; Bond et al. 2010) or for the overall system (Sirko et al. 2004a). The tangential velocity dispersions not only provide the information of the anisotropy of the stellar population (through Equation 1) but together with  $\sigma_r$  also helps to measure the mass distribution of the Galaxy.

We estimate the tangential velocity dispersions ( $\sigma_{\theta}$  and  $\sigma_{\phi}$ ) using CME with  $n_{\text{bin}} = 1200$  stars. Given the quality of the data, we are only able to measure  $\sigma_{\theta}$  and  $\sigma_{\phi}$  out to  $\sim 25 \text{ kpc}$ . Our estimates of  $\sigma_{\theta}$  and  $\sigma_{\phi}$  are shown in Figure 3b,c by the black dots with error bars. For uniformity, we also estimate the  $\sigma_r$  with this binning scheme and this is shown (only out to  $\sim 25 \text{ kpc}$ ) in Figure 3a by the black dots with error bars.

In general the tangential components  $\sigma_{\theta}$  and  $\sigma_{\phi}$  near the solar neighborhood are found to be comparatively lower ( $\sigma_{\theta} = 85_{-9}^{+8} \text{ km s}^{-1}$ ,  $\sigma_{\phi} = 95_{-8}^{+8} \text{ km s}^{-1}$ ) than the radial dispersion  $\sigma_r$ . It can be seen in the Figure 3b and c that there is a sharp rise in the values of  $\sigma_{\theta}$  and  $\sigma_{\phi}$  at  $r = 17 \text{ kpc}$ . Beyond this  $\sigma_{\phi}$  falls whereas  $\sigma_{\theta}$  rises, given the large uncertainties and low number of independent bins it is unclear if this is a real or a spurious trend.

By substituting the estimates of the tangential and the radial velocity dispersions obtained using CME ( $n_{\text{bin}} = 1200$ ) from the above analysis into Equation (1) we compute the corresponding values of the anisotropy constant in the respective bins. As shown in Figure 3d, the halo within 12

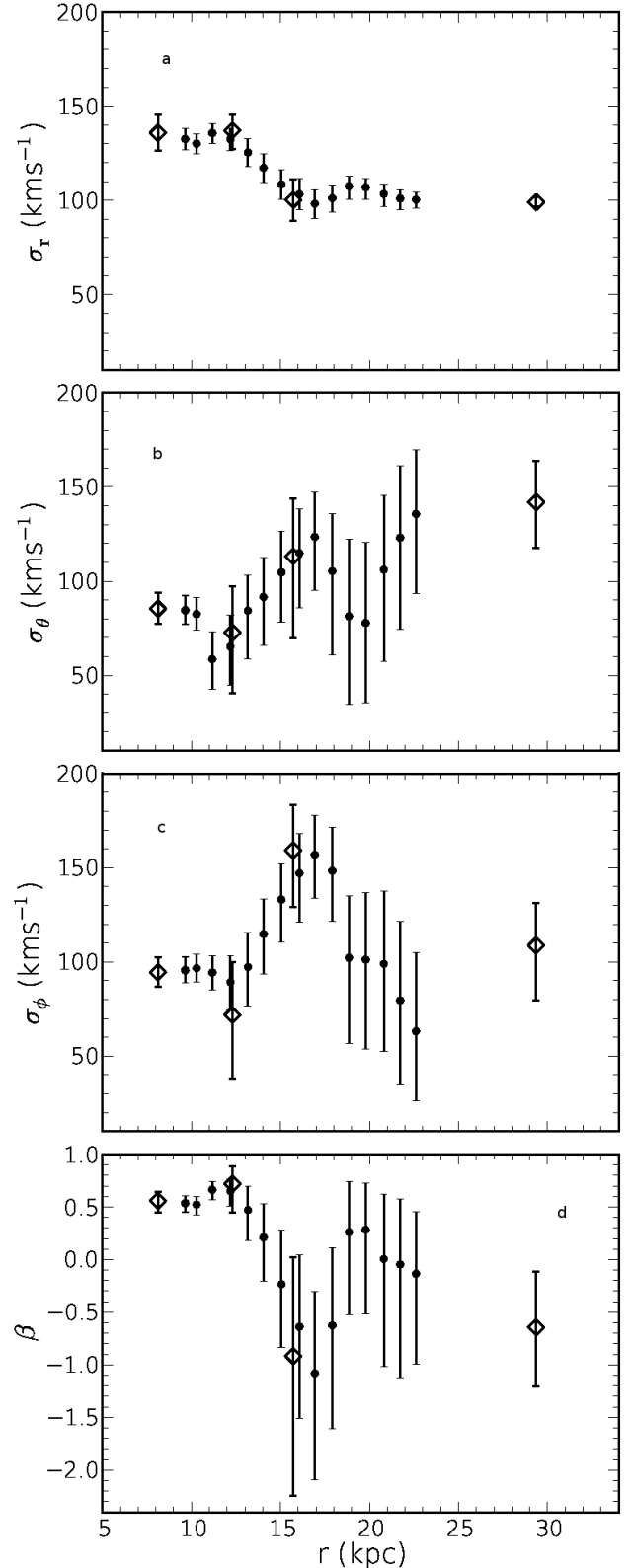


**Figure 3.** Velocity Dispersions and Anisotropy profiles: From top to bottom is  $\sigma_r$ ,  $\sigma_{\theta}$ ,  $\sigma_{\phi}$ , and  $\beta$  profiles of the stellar halo estimated in the radial bins. The diamond and the round markers are the results for the two binning schemes, namely the EPE and the CME respectively. Note that the last radial bin marked with the open diamond contains the remaining stars. The diamond markers in plot (a) is just shown for the ease of comparison.

kpc has  $\beta \sim 0.5$  whereas the outer halo beyond the turn-off point is nearly isotropic. We discover a significant drop in the  $\beta$  profile at  $r = 17$  kpc. Here the halo is strongly tangential with  $\beta = -1.2$ . We later confirm that the trend observed in anisotropy is neither due to the manifestation of the systematics introduced by the chosen model (§3.3) nor due to presence of the halo substructures (§3.4). It is also shown in the appendix B that assumed  $v_{\text{LSR}}$  and  $R_{\odot}$  have negligible effects upon these estimates. The probable reasons for this sudden turn-over in the properties of the halo are discussed in the conclusion.

We know that the consecutive CME bins overlap in radius and thus the dispersion profiles demonstrated in Figure 3 is a smoothed version of the actual dispersion profiles of the halo. However, to check for any systematic associated with the choice of the binning scheme, we also estimate  $\sigma_r, \sigma_{\theta}, \sigma_{\phi}$ , and  $\beta$  in traditional equi-populated (EPE) bins ( $n_{\text{bin}} = 700$ ). The measured values in these bins are shown by the diamond points in Figure 3. If the number of stars per bin is less than 700 it is difficult to constrain  $\sigma_{\theta}$  and  $\sigma_{\phi}$ . Even with  $n_{\text{bin}} = 700$  we were able to constrain the tangential motion only till 16 kpc (first three diamond points). Hence, we construct the last bin by grouping all the stars beyond 16 kpc into one bin (rightmost diamond point). More importantly, with this binning scheme we are only interested to see whether we obtain the corresponding dip or rise (depending on the parameter of interest) seen in Figure 3 or not. We find that except for the right-most diamond points all of other diamond points in the figure are in agreement with our previous estimates of the dispersions (given by black dots). The rightmost diamond points are calculated in a huge bin with more than 50% of the total sample. Particularly for  $\sigma_{\theta}, \sigma_{\phi}$  and  $\beta$  given the non-monotonic trend they have, hence we do not claim the last diamond point is the correct estimate of anisotropy at  $r \sim 35$  kpc.

None of the uncertainties quoted in the above estimates of  $\sigma_r, \sigma_{\theta}$  and  $\sigma_{\phi}$  include the uncertainties in distances and radial velocities. As mentioned earlier, the errors in distance and radial velocity are quite small, and convolving the model (Equation 4) with the error functions should not change the results.

### 3.3. $\beta(r)$ from fitting Distribution Function ( $f(E, L)$ )

It would be interesting to see whether the  $\beta$  profile presented above, in particular the dip seen at  $r = 17$  kpc, is an artifact of our chosen model (GVE) or a real inherent feature of the Galactic halo. In order to pursue it, here we explore the effect of the chosen model on the determination of the velocity anisotropy ( $\beta$ ). For the comparative study, the alternative model we choose is the D11 DF (Equation 3). We consider anisotropy ( $\beta$ ) and potential ( $= \Phi_0 r^{-\gamma}$ ) as free model parameters and constrain them using the maximum likelihood method.

First, we compare the theoretical properties of the DFs at our disposal namely, GVE and D11 DF. In Figure 4 we plot the theoretical LOSVDs of models along two separate line-of-sights. We also show the LOSVDs in Figure 4 for two different distances representing the inner halo ( $d = 15$  kpc, given by red lines) and the outer halo ( $d = 50$  kpc, given by blue lines). For the inner-halo we assume  $\alpha = 2.4$  and assign radially biased anisotropy ( $\beta = 0.4$ ) whereas for the outer-halo we assume  $\alpha = 4.5$  and assign tangentially biased anisotropy ( $\beta = -2.5$ ) in accordance to Watkins et al. (2009) and Deason et al. (2011b) estimates for  $\alpha$ . Note, the density normalization at

the break radius ( $r = 27$  kpc) is assumed to be equal. For the assumed constant potential the solid lines in Figure 4 (both left, right panels) are the LOSVDs obtained by adopting the D11 model and dashed lines are the LOSVDs of our GVE model. Recall that our model does not take  $\beta$  directly but demands the information of the velocity dispersion components ( $\sigma_r, \sigma_{\theta}, \sigma_{\phi}$ ) individually. To make the LOSVDs obtained from both the models comparable we estimate  $\sigma_r, \sigma_{\theta}, \sigma_{\phi}$  from the set of values of  $\beta, \alpha, \Phi_0$  and  $\gamma$  chosen to obtain LOSVDs of D11 DF. For an assumed potential power law we use Equation (8) to first calculate  $\sigma_r$ , to put in our model. For an assumed  $\beta$ , substituting this  $\sigma_r$  in Equation (1) gives the corresponding value for  $\sigma_t (= \sqrt{\sigma_{\theta}^2 + \sigma_{\phi}^2})$ . It can be seen in the figure that for all the four cases LOSVDs obtained from both the models match well. Naively, from these perfect matches of the LOSVDs at different line-of-sights and distances it can be anticipated that the estimation of  $\beta(r)$  with both models should also match.

Now we estimate the  $\beta(r)$  using exactly the same sample of BHB stars in same radial bins as in §3.2 (CME,  $n_{\text{bin}} = 1200$ ) but with D11 DF. Blue points in Figure 5 demonstrate the  $\beta$  profile obtained by fitting D11 DF. Here we use brute-force grid based analysis to constrain the model parameters  $\beta, \Phi_0$  and  $\gamma$ . To facilitate the comparison our estimates from Figure 3d are over plotted in Figure 5 and are shown by the black points. From Figure 5 it can be seen that within the range of uncertainties the measured values of  $\beta$  with both models (D11 DF and GVE model) agree. However, a slight bias can be seen in the sense that  $\beta$  obtained from GVE DF is in general higher. The reason for this discrepancy lies in the fact that  $\beta$  obtained from the D11 DF has a dependence on  $\alpha$ . Hence, unless the underlying  $\alpha$  value of the sample is exactly known, a mismatch is expected. The estimated value of  $\beta$  increases with the adopted value of  $\alpha$  (see Fig-3 D11). This suggests that the actual value of  $\alpha$  is even higher than the one that is adopted here (2.4).

In order to give an estimate of the quality of constraints obtained from the likelihood analysis we display the likelihood contours in the parameter space in the top left and bottom two plots in Figure 6 for a bin centered at  $r = 16.93$  kpc where the maximum dip in the  $\beta$  profile was seen in Figure 5. Additionally, in the corresponding bin, the top right plot in figure demonstrates the posterior distributions of the model parameters  $\sigma_r, \sigma_{\theta}$  and  $\sigma_{\phi}$  of the GVE model obtained from  $5 \times 10^5$  MCMC random walks. It can be seen that even at a distance of just twice of  $R_{\odot}$ ,  $\sigma_{\theta}$  and  $\sigma_{\phi}$  distributions are quite broad as compared to  $\sigma_r$  distribution; this is the reason for the large uncertainty in the value of  $\beta$  as we move outwards in  $r$ .

### 3.4. Effect of the halo substructures

There is now enough observational evidence to suggest that the stellar halo is highly structured particularly as one moves outwards into the halo (Bell et al. 2008). Using clustering algorithms on simulated N-body stellar halos, Sharma et al. (2011b) find that the fraction of material in substructures increases monotonically as a function of distance from the center and at around 65 kpc can be as high 50%. Hence, while studying the kinematic properties of the halo should we include the substructures or exclude them? If the kinematic properties of a sample are dominated by a few massive accretion events then one should exclude them. However, in spite of being highly structured if the sample is a superposition of large number of events with none of them being in-

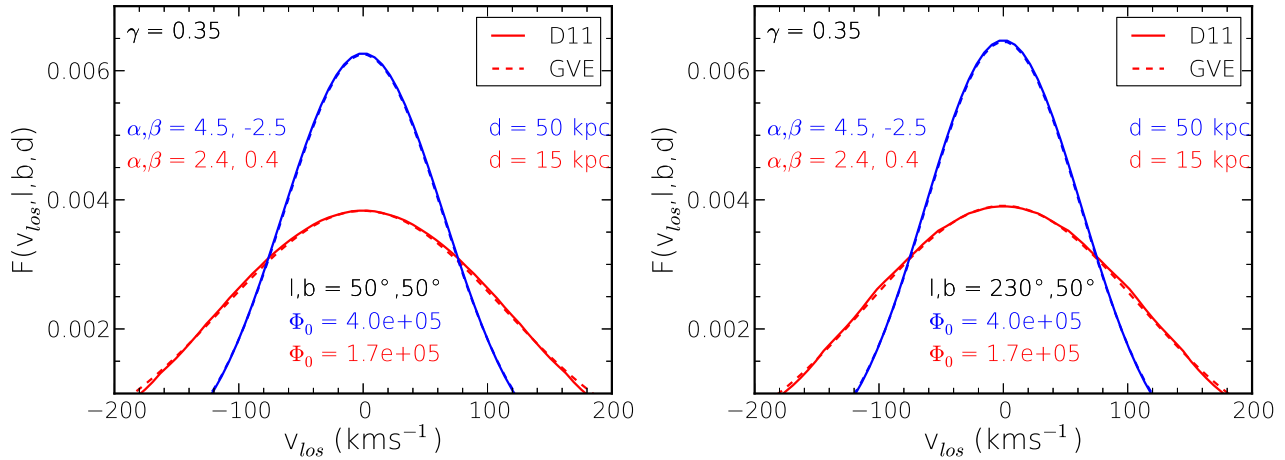


**Figure 4.** Comparison of the marginalized DF given by Equation (5) obtained for D11 models and GVE distribution along two different line-of-sights. Solid line is the LOSVD for the D11 DF whereas dashed line is the LOSVD for the GVE model. Red and blue lines represent LOSVD for two different distances ( $d$ ) 15 kpc and 50 kpc respectively. The potential is assumed to be a power law given by  $\Phi_\circ r^{-\gamma}$ , where  $\Phi_\circ$  (in  $\text{km}^2\text{s}^{-2}$ ) is the potential normalization. Potential slope ( $\gamma$ ) is assumed constant and equal to 0.35 for all the cases. Left: LOSVD along  $(l, b) = (50^\circ, 50^\circ)$  Right: LOSVD along  $(l, b) = (230^\circ, 50^\circ)$ .

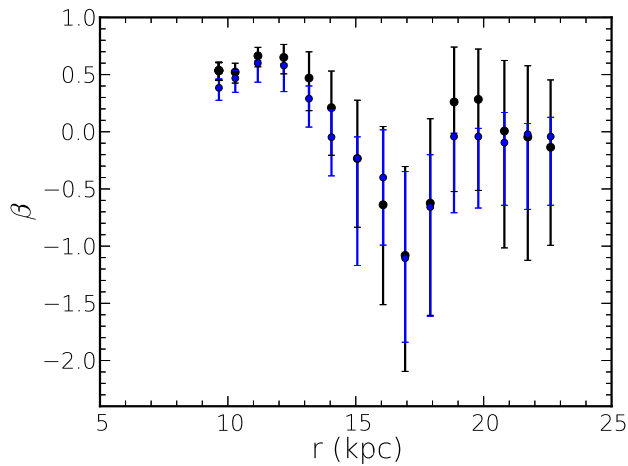


**Figure 5.** Anisotropy ( $\beta$ ) estimates in the CME using D11 model (blue points) and GVE model (black points). Each bin consists of 1200 stars. Anisotropy estimates with GVE distribution is done with MCMC technique whereas estimates with D11 model is done with the brute-force grid based analysis. Assigned asymmetric uncertainties are  $1\sigma$  confidence intervals obtained from likelihood fitting.

dividually too dominant then it is best to include them. Results of Sharma et al. (2011b) on simulated halos show that for the range of radii that spans our BHB stars ( $r < 40$  kpc) the amount of material in substructure should be less than 20%. So we expect the substructures to have a minor effect on the kinematic properties that we have derived. However, it is still important to check if this is true.

To study the effect of substructures on our estimation of the dispersions we mask two prominent features of the halo that contaminate our sample, namely, the Sagittarius stellar stream and the Virgo over-density. Cuts we impose include the Lambert Equal-Area projection cut as given in Bell et al. (2008) and an additional cut in equatorial coordinates (RA and DEC) suggested by Deason et al. (2011b). We mask the region within  $0 < X$  (abscissa of the equal-area projection)  $< 30$ , where  $X$  is given by  $63.63961[2(1-\sin b)]^{1/2}$ ; and  $0^\circ < \text{RA} < 50^\circ$ , and  $-30^\circ < \text{DEC} < 0^\circ$ , which is purely a geometric cut. These stringent cuts reduce our final sample to 2975 stars. A proper phase-space masking of these structures will be revised

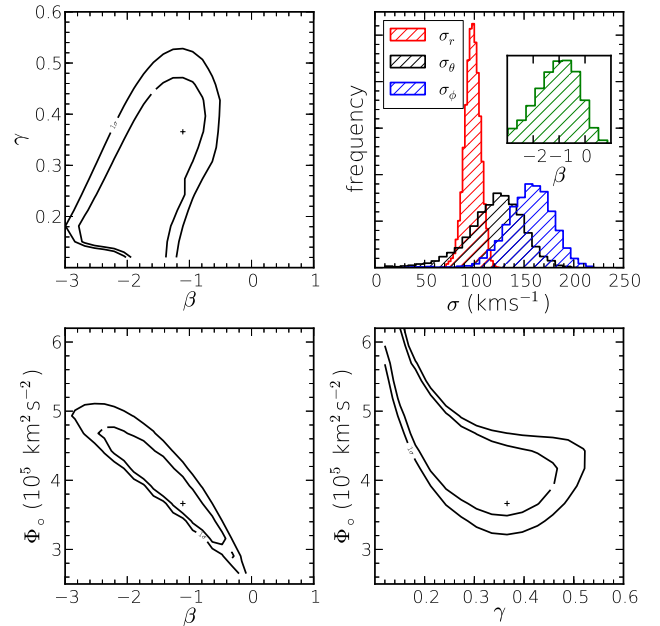


**Figure 6.** The posterior distributions of the parameters for bin centered at  $r = 16.93$  kpc. Upper Right: The posterior distributions of the GVE model parameters,  $\sigma_r$ ,  $\sigma_\theta$  and  $\sigma_\phi$ , obtained with  $5 \times 10^5$  MCMC random walks. In the inset is the derived distribution of the  $\beta$  parameter. Upper Left and Lower panels: The joint likelihood contours of the D11 model parameters  $\beta$ , potential normalization ( $\Phi_\circ$ ) and potential slope ( $\gamma$ ) are obtained with brute force analysis. The outer contour displays  $1\sigma$  region whereas the inner contour demonstrates a region of 50% confidence interval. Cross hair corresponds to the point where the likelihood is maximum.

in the future work.

In Figure 7 we present our result obtained after masking the substructures. As masking reduces the sample size almost by half, we employ CME with  $n_{\text{bin}} = 500$  stars only, instead of  $n_{\text{bin}} = 1200$  as was done earlier with unmasked data, to avoid excessive smoothing of the estimated profiles. Figure 7 shows that the masking of substructures have little effect on the estimation of velocity dispersion profiles, the  $\beta$  profile is almost unchanged. This alleviates the concern that perhaps the turnover points in the velocity dispersion profiles and the dip in  $\beta$  profile, seen in Figure 3, in the region  $r = 13 - 18$  kpc could

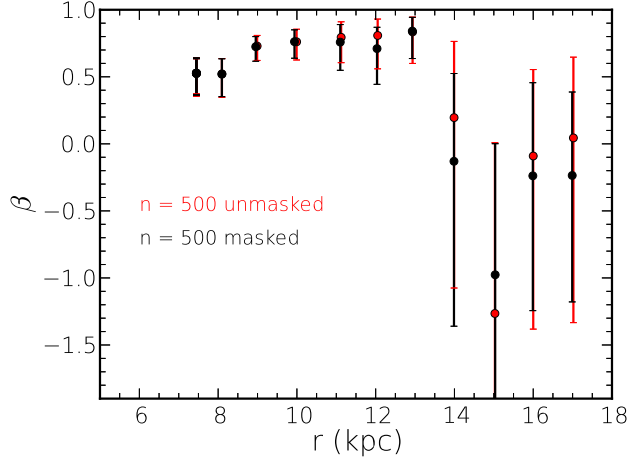


**Figure 7.** Effect of the halo substructures, namely, the Sagittarius stellar stream and the Virgo over-density. Each CME bins contain 500 stars. Black and red points are our result for the masked and the unmasked halo respectively. Error bars quoted are  $1\sigma$  credibility interval.

be due to the dominance of halo substructures.

#### 4. COMPARISON OF ANISOTROPY ESTIMATES IN D11 AND D12 RADIAL BINS

In their recent work D11 and D12 fit a distribution function of the form given by Equation (3), to the BHB samples obtained from SEGUE survey in order to estimate the model parameters. The models adopted are constant anisotropy models given by Equation (2). In D11, the potential is assumed to be a power law ( $\propto r^{-\gamma}$ ) and with a constant index ( $\gamma = 0.35$ ). Later in D12, they break the degeneracy present in their model and consider the potential normalization ( $\Phi_0$ ), potential slope ( $\gamma$ ) and anisotropy ( $\beta$ ) as free parameters. Note, in D11 there is an additional parameter specifying rotation (odd part of the DF) but this was dropped in D12, as they were not focusing on rotation. The methodology applied to measure the model parameters is similar to ours which involves marginalizing the DF over the tangential velocities to derive the line-of-sight velocity distribution (LOSVD); fitting the LOSVD to the data using the maximum likelihood method and in return obtaining the best estimates of the model parameters.

##### 4.1. Anisotropies of inner and outer halo by D11

D11 study the rotation and the anisotropy of the BHB samples taken from SDSS Data Release 7 (Abazajian et al. 2009). First, in order to construct the sample used by them we query SDSS DR7 database to select the candidate BHB stars using the color and the stellar parameters ranges given in D11. Like them we also mask the Sagittarius dwarf galaxy which reduces the original sample size by 40% to  $\sim 3500$ .

D11 measure the anisotropy of the halo in radial and metallicity bins. In the inner halo ( $10 < r/\text{kpc} < 25$ ) both metal-rich ( $[\text{Fe}/\text{H}] > -2$ ) and metal poor ( $[\text{Fe}/\text{H}] < -2$ ) stars are found to be tangential with  $\beta \sim -1.2$  and  $\sim -0.2$  respectively. In the corresponding metallicity bins, the outer halo ( $25 < r/\text{kpc} < 50$ ) is found to be radial with  $\beta$  of  $\sim 0.4$  and  $\sim 0.5$  respectively. Since they do not give the estimates of  $\beta$  in combined metallicity bins for the inner and outer halo, we estimate them here using the same methodology as adopted by them. For the inner halo we find  $\beta = -0.62$  (tangential) and for the outer halo we find  $\beta = 0.41$  (radial). These estimates are consistent with D11 results, if we combine their low and high metallicity  $\beta$  values in each radial bin.

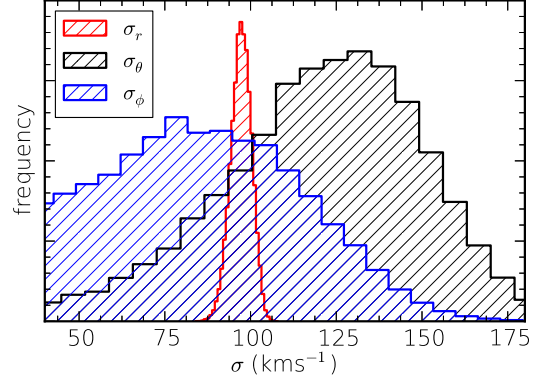


**Figure 8.** Posterior distribution of velocity dispersions for D12 data set within  $16 < r/\text{kpc} < 48$  using a GVE model. The value of  $v_{\text{LSR}}$  here is taken to be  $240 \text{ km s}^{-1}$  to keep it same as in D12.

The inner halo within the solar vicinity has been found to be radial in studies of halo subdwarfs by Smith et al. (2009b) and in studies of  $10^5$  main sequence stars by Bond et al. (2010) (see also Figure 3d). Hence, a tangential inner-halo as predicted by D11 is surprising. The first thing to check is if the D11 result is due to some of the assumptions made by them. For example, in D11 the logarithmic density slope was assumed to be constant and equal to  $-3.5$ . Later on Deason et al. (2011b) conducted a detailed analysis of the BHB stars to estimate their density profile and found that the profile is of the form of a broken power law, the inner-halo ( $< 27 \text{ kpc}$ ) having a profile index of  $-2.3$  and the outer halo having a profile index of  $-4.6$ . This is in good agreement with the findings of Watkins et al. (2009) that the halo within  $25 \text{ kpc}$  has the profile index  $-2.4$  and beyond which it is steeper with an index  $-4.5$ .

If we update the density profile index in the D11 case with the above values then we expect the inner halo which is already tangential to become even more tangential and the outer halo which is already radial to become even more radial. This is because  $\beta$  has a dependence on the adopted value of  $\alpha$  as shown by D11 (Figure 5). In general  $\beta$  increases with an increase in the adopted value of  $\alpha$ . Another effect that can potentially bias the results is the fact that the potential parameters ( $\Phi_0, \gamma$ ) have been kept fixed in the D11 analysis, i.e., the degeneracy between  $\beta$  and potential has not been broken. After analyzing data in finer bins and breaking the degeneracy among the model parameters we do see that in Figure 5 the inner halo is radial (from §3.3) as was also found with the GVE model. Hence the assumption of a fixed potential can bias the estimation of  $\beta$ . However, a much more apparent reason for the discrepancy is as follows. Clearly, from Figure 3 the radial bin from  $10\text{-}25 \text{ kpc}$  will encompass the stars within  $13\text{-}17 \text{ kpc}$  which are predominantly tangential. Since the probability density of stars in radius also peaks at around  $16 \text{ kpc}$  (see Figure 1) we anticipate the overall  $\beta$  to be tangential. To conclude, the tangential behavior of the inner-halo seen by D11 is most likely due to the large radial bin size adopted by them.

##### 4.2. Anisotropy at $16 < r/\text{kpc} < 48$ seen by D12

D12 re-calibrate the distances of BHB stars using the color-magnitude relation given by Deason et al. (2011b) and then select stars within  $16 \lesssim r/\text{kpc} \lesssim 48$  (1933 stars) from Xue et al. (2011) BHB samples. They fit the D11 model to study the nature of  $\beta$  in the outer halo. Unlike D11, as mentioned previously here they break the degeneracy present in



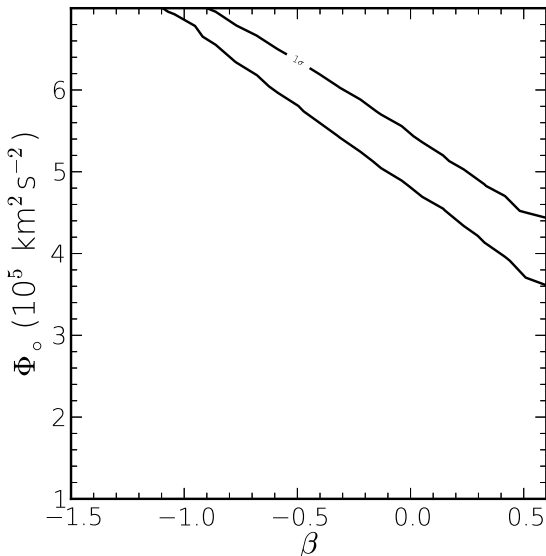


**Figure 9.** Maximum likelihood analysis of the anisotropy parameter,  $\beta$ , for stars in the radial bin  $35 < r/\text{kpc} < 84$ . Solid black lines are the  $1\sigma$  confidence region. Density and potential slopes are taken to be 4.5 and 0.35.

their model and consider the  $\beta$ ,  $\Phi_o$  and  $\gamma$  as free parameters. Thus while they fit the model they simultaneously estimates all three parameters. They find  $\beta = 0.4^{+0.2}_{-0.2}$  for  $\alpha = 4.6$ . Using a model allowing for oblateness ( $q = 0.59$ ) they find  $\beta = 0.5^{+0.1}_{-0.2}$ . If we apply the GVE distribution function to stars in the range  $16 < r/\text{kpc} < 48$  we find  $\beta = -0.14^{+0.52}_{-0.66}$  ( $\sigma_r = 97.3^{+2.9}_{-3.0} \text{ km s}^{-1}$ ,  $\sigma_\theta = 122.7^{+26.4}_{-33.0} \text{ km s}^{-1}$  and  $\sigma_\phi = 78.5^{+34.3}_{-40.7} \text{ km s}^{-1}$ ). This more or less looks like the mean value of  $\beta$  in this range (see Figure 5) provided we take into account the fact that the number density of stars peak at around  $r = 16$  kpc. Although the D12 value is still within our  $1\sigma$  region, our predicted value is lower than D12. It can be seen from Figure 5 that  $\beta$  is not constant in the range  $16 < r/\text{kpc} < 23$ . It increases from being tangential to isotropic. Using the D11 DF also gives similar result (§3.3). Beyond this range we cannot directly measure  $\beta$ , but by deriving a best fit circular velocity profile and making use of  $\sigma_r$  profile which is available till  $r = 56$  kpc we can predict  $\beta$ , and this is returned to in section 5. However, an assumption about  $\alpha$  also has to be made. Beyond,  $r > 27$  kpc the density slope has been shown to change from  $-2.4$  to  $-4.5$ . Adopting a steeper density slope increases the value of  $\beta$ . For  $\alpha = 4.5$  we find  $\beta \sim 0.5$  for  $r > 27$  kpc; this is more in agreement with D12. To conclude, the D12 value of  $\beta = 0.4$  for  $16 < r/\text{kpc} < 48$ , although derived for a sample which is dominated by stars within  $r < 27$  kpc, is not appropriate for the range  $18 < r/\text{kpc} < 23$ , instead it is correct for the range  $23 < r/\text{kpc} < 48$ .

Finally, we check how best we can measure  $\beta$  in the outer most parts,  $35 < r/\text{kpc} < 84$ , using the D11 DF and the data in hand. This region consists of 762 stars, and we assume  $\alpha = 4.5$  and  $\gamma = 0.35$  and repeat the analysis as in D12. The likelihood distributions of model parameters are shown in Figure 9. The mass-anisotropy degeneracy is clearly visible here, suggesting that it is very difficult to directly measure  $\beta$  unless an explicit or implicit assumption about the potential is made.

## 5. CIRCULAR VELOCITY CURVE OF THE GALAXY

Here we use the measured values of  $\sigma_r(r)$  and  $\beta(r)$  from our analysis given in Figure 3 to determine the circular velocity curve of the Galaxy ( $v_{\text{circ}}$ ) through the Jeans equation (Equation 7). Besides anisotropy and radial velocity dispersion information we also need to adopt some density profile for the tracer population but not of the spectroscopic sample. We adopt a value of  $\alpha = 2.4$  as suggested by recent works of Watkins et al. (2009) and Deason et al. (2011b), for the range of distance explored here ( $r < 25$  kpc). The blue dots with error bars in Figure 10 are our estimates of  $v_{\text{circ}}$  using CME with  $n_{\text{bin}} = 1200$ . The uncertainties on  $v_{\text{circ}}$  were computed using a Monte Carlo based scheme from uncertainties in  $\sigma_r$  and  $\beta$ . The leftmost and rightmost points have comparatively larger error bars as compared to intermediate points. For the leftmost point the large error bar is mainly due to large error in the value of  $\sigma_r$ . On the other hand, for the right-most point the large error bar is mainly due to large error in the values of  $\sigma_\theta$  and  $\sigma_\phi$ .

In Figure 10 it can be seen that the circular velocity profile derived from our analysis (blue points) display prominent features. We now check if such features are also observed in other studies using tracers other than BHB stars. For this we over-plot  $v_{\text{circ}}$  compiled by Sofue et al. (2009) as black dots, obtained from several references (Burton & Gordon 1978; Blitz et al. 1982; Clemens 1985; Fich et al. 1989; Honma & Sofue 1997b,a; Honma et al. 2007; Demers & Battinelli 2007). Further details about the source of each individual point can be found in Sofue et al. (2009) and references therein. Note,  $v_{\text{circ}}$  values of Sofue et al. (2009) are computed for  $(R_\odot, v_{\text{LSR}}) = (8.0 \text{ kpc}, 200.0 \text{ km s}^{-1})$ . Correcting the  $v_{\text{circ}}$  for our adopted values of  $(R_\odot, v_{\text{LSR}}) = (8.5 \text{ kpc}, 220.0 \text{ km s}^{-1})$  is beyond the scope of this work and hence we simply over-plot these published values in Figure 10. It can be seen there is a prominent dip at 9 kpc in the Sofue et al. (2009) compiled  $v_{\text{circ}}$  profile. They explain this dip by introducing massless rings on top of a disk with exponential surface density. We also find a similar dip in our  $v_{\text{circ}}$  profile but at around 10-12 kpc. The slight shift in the position of dip could be due to large width of our bins and also due to the fact that unlike Sofue et al. (2009), who measure  $v_{\text{circ}}$  in the mid-plane of the Galaxy, we measure  $v_{\text{circ}}$  over a spherical shell that intersects with the SDSS footprint.

We now estimate the mass of the dark matter halo of the Milky Way, assuming a three component model of the Galaxy consisting of the bulge, the disk, and the halo. The bulge is modeled as a Hernquist sphere and the disk is assumed to follow an exponential profile (Xue et al. 2008). The parameters for the bulge and disk are taken from Sofue et al. (2009) and are kept fixed. Although Sofue et al. (2009) use massless rings, we here have ignored them since our main aim is to fit the dark matter halo. We model the dark matter halo using the NFW (Navarro et al. 1996) density profile. Here we consider both the halo and the bulge to be spherically symmetric. The non-axisymmetric effect due to a bar shaped bulge is neglected here. Potentials for bulge, halo, and exponential disk can be expressed as,

$$\Phi_{\text{disk}}(r) = -\frac{GM_{\text{disk}}(1 - e^{-r/b})}{r}, \quad (10)$$

$$\Phi_{\text{bulge}}(r) = -\frac{GM_{\text{bulge}}}{r+a}, \quad \text{and} \quad (11)$$

$$\Phi_{\text{NFW}}(r) = -\frac{GM_{\text{vir}} \ln(1 + rc/R_{\text{vir}})}{g(c)r} \quad (12)$$

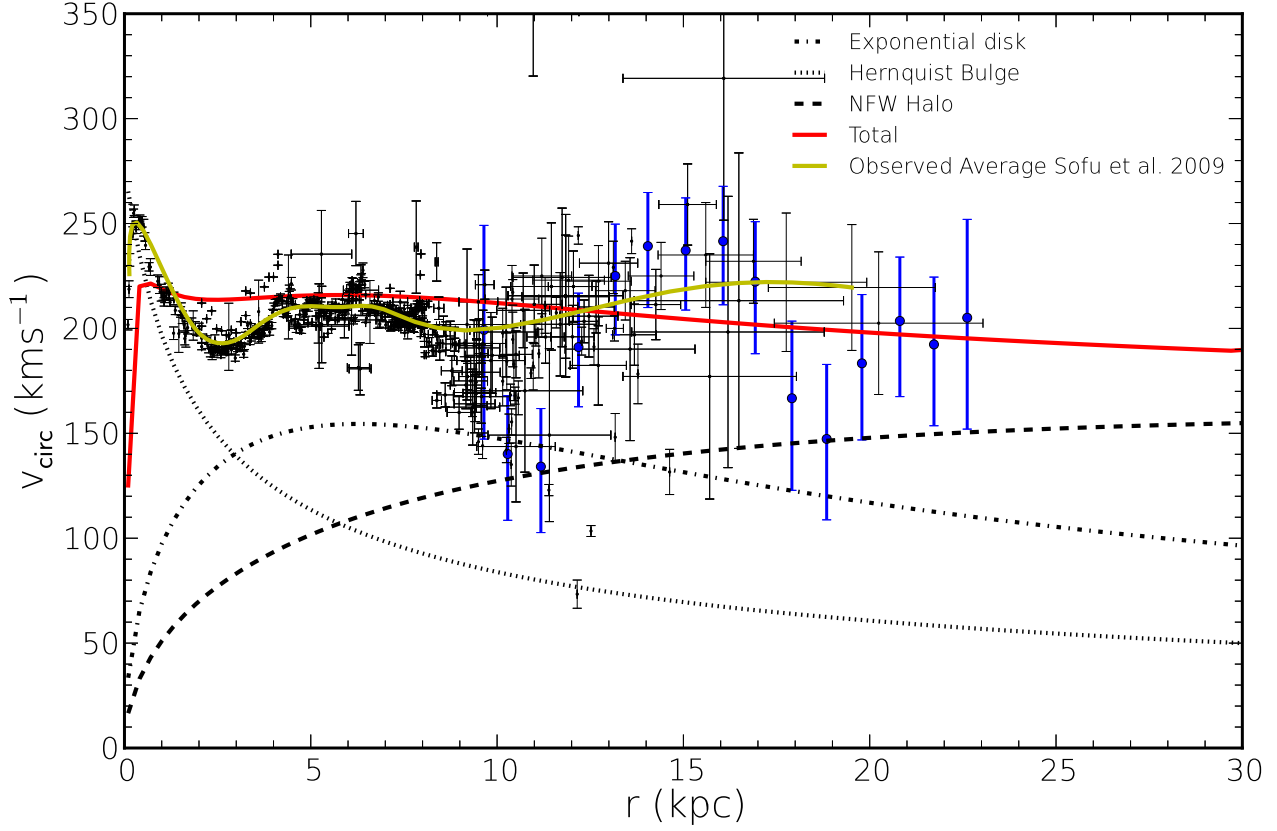


**Figure 10.** Circular velocity curve of the Galaxy and their individual components along a galactocentric distance ( $r$ ). The blue marker represents the value of  $v_{\text{circ}}$  obtained in the CME bins in  $r$ . Red solid line is our fit of the total potential. Black dotted and dotted-dashed lines are the fixed disk and the bulge circular velocity profile for set of adopted values of masses and scale radii. Dashed line is the fitted NFW profile. Black dots with error bars are the collated  $v_{\text{circ}}$  values given by Sofue et al. (2009) whereas yellow solid line is the average of the given observed values.

where  $M_{\text{disk}} = 6.5 \times 10^{10} M_{\odot}$ ,  $b = 3.5$  kpc,  $M_{\text{bulge}} = 1.80 \times 10^{10} M_{\odot}$ , and  $a = 0.5$  kpc (Sofue et al. 2009).

Note, the disk potential as given by Equation (10) is spherically symmetric. It means the disk is considered to be a spherical body with exponential surface density fall-off. To get an idea on the error that is incurred due to the assumption of the disk as a spherical body with the mass same as the flattened disk we refer reader to Binney & Tremaine (2008) (Figure 2.17). Roughly the maximum error in  $v_{\text{circ}}$  is 13%, which is at a distance about twice of the disk scale length. However, at the larger distances along the mid-plane the discrepancy is smaller. In the general case of triplanar symmetry (elliptic disk), in reality, the disk potential has to be the function of both polar and azimuthal coordinates and in the special case of axial symmetry (circular disk) it has to be the function of sole polar coordinates, in addition to the radial coordinates ( $r$ ). We here use the spherically symmetric form for two reasons. Firstly, we make use of the spherical form of the Jeans equation given by Equation (7) which demands a spherical potential. Secondly, it is to ease the comparison with earlier studies, e.g., Xue et al. (2008), that adopt a similar definition. However, later on we consider a 3D disk potential and discuss its consequences on the estimation of mass. The function  $g$  in NFW potential is given by

$$g(c) = \ln(1+c) - \frac{c}{1+c}$$

and

$$R_{\text{vir}} = \left( \frac{2M_{\text{vir}}G}{H_0^2 \Omega_m \Delta_{\text{th}}} \right)^{1/3}.$$

The total potential  $\Phi(r)$  of the Galaxy is then simply

$$\Phi(r) = \Phi_{\text{bulge}}(r) + \Phi_{\text{disk}}(r) + \Phi_{\text{NFW}}(r) \quad (13)$$

We adopt the value of Hubble constant,  $H_0 = 70.4$   $\text{kms}^{-1}\text{Mpc}^{-1}$ ,  $\Omega_m = 0.3$  (Komatsu et al. 2011), and  $\Delta_{\text{th}} = 340$  (Bryan & Norman 1998).

A NFW halo has two free parameters the mass  $M_{\text{vir}}$  and the concentration  $c$ . Since we do not have enough data points spanning a wide range in radius, we avoid fitting both the parameters simultaneously. Instead we use the concentration mass relation,

$$c = 327.3M_{\text{vir}}^{-0.12}, \quad 10^{11} \leq M_{\text{vir}}/M_{\odot} \leq 10^{13}, \quad (14)$$

as has been reported in N body simulations of dark matter halos (Macciò et al. 2007).

Finally, we can derive the resultant circular velocity ( $v_{\text{circ}}$ ) from the total potential (Equation 13) by computing  $(rd\Phi/dr)^{1/2}$ . We fit the obtained theoretical rotation velocity curve to our observed values of  $v_{\text{circ}}$  shown by the blue dots in Figure 10, and the red line is our best fit circular velocity curve. The  $v_{\text{circ}}$  profiles for the different components are also shown separately. The dashed black line is the corresponding best fit NFW halo profile. The best fit value for the fit parameter,  $M_{\text{vir}}$ , for our three component baryon and dark matter

mass distribution is  $0.9_{-0.3}^{+0.4} \times 10^{12} M_{\odot}$ . The corresponding values of  $R_{\text{vir}}$  and  $c$  derived from the best fit value of  $M_{\text{vir}}$  are  $249_{-31}^{+34}$  kpc and  $12.0_{-0.5}^{+0.6}$  respectively. We estimate the mass of the Galaxy within  $r \lesssim 25$  kpc to be  $2.1 \times 10^{11} M_{\odot}$ . Assuming a functional form for  $P(v_{\text{los}}/v_{\text{circ}})$  obtained from simulations Xue et al. (2008) derive the  $v_{\text{circ}}$  from the  $v_{\text{los}}$  of BHB stars. The derived  $v_{\text{circ}}$  is then used to estimate the virial mass of the dark matter halo. They find  $M_{\text{vir}} = 0.91_{-0.18}^{+0.27} \times 10^{12} M_{\odot}$  which is in good agreement with our result, note uncertainties are however, slightly larger in our estimates. Since unlike them we do not make any assumption about the functional form of  $P(v_{\text{los}}/v_{\text{circ}})$ .

Here we study the effect of chosen disk models for which we consider more realistic three-dimensional potential for the disk by Miyamoto & Nagai (1975), which holds for the special case of a circular disk. The expression for this potential is given by

$$\Phi_{\text{disk}}(R, z) = -\frac{GM_{\text{disk}}}{\sqrt{R^2 + (a + \sqrt{z^2 + b^2})^2}}. \quad (15)$$

Here again, the disk parameters are obtained from the best fit values along the galactic mid-plane ( $z = 0$ ) which reproduces  $v_{\text{circ}}(R)$  profile for Sofue et al. (2009) razor-thin exponential disk (Freeman 1970) i.e.  $b = 0.0$  kpc<sup>2</sup>. Hence the best fit value for the disk parameter  $a = 2.5$  kpc whereas mass  $M_{\text{disk}} = 6.5 \times 10^{10} M_{\odot}$  is taken same as in Sofue et al. (2009). Since we assume the disk potential to be three-dimensional here, for the purpose of computing the total  $v_{\text{circ}}$  we consider the component of force along the radial direction ( $r$ ) only. The bulge and the halo models are kept same as earlier. The best fit values for the NFW halo parameters with the updated disk model is found to be  $M_{\text{vir}} = 1.2_{-0.4}^{+0.5} \times 10^{12} M_{\odot}$  with  $R_{\text{vir}} = 274_{-30}^{+35}$  kpc. Instead if we consider the total magnitude of the force in order to compute the  $v_{\text{circ}}$  we estimate  $M_{\text{vir}}(R_{\text{vir}} = 269_{-32}^{+34} \text{ kpc}) = 1.1_{-0.4}^{+0.5} \times 10^{12} M_{\odot}$ . Historically, large values of  $a$  have been assumed while modeling the disk (Wolfire et al. (1995); Bland-Hawthorn (2009)). We find that this leads to a much more massive dark matter halo– for  $a = 4.5$  kpc we find  $M_{\text{vir}}(R_{\text{vir}} = 299_{-33}^{+36} \text{ kpc}) = 1.6_{-0.5}^{+0.6} \times 10^{12} M_{\odot}$  and for  $a = 6.5$  kpc we find  $M_{\text{vir}}(R_{\text{vir}} = 321_{-34}^{+35} \text{ kpc}) = 1.9_{-0.6}^{+0.7} \times 10^{12} M_{\odot}$ .

There are few things which have insignificant or unexplored effects on our mass estimation e.g. we do not take into account the mass of the super-massive black hole, which is  $\sim 4 \times 10^6 M_{\odot}$  (Schödel et al. 2002; Eisenhauer et al. 2005; Gillessen et al. 2009), and is approximately 1/1000 of the mass of the bulge. Moreover, its effect is like that of a point mass and can be easily absorbed into the bulge mass. Another effect that is not considered is the tidal effect on the primary object that has been qualitatively studied to find the mass ratio between the Galaxy and M31 (Baiesi Pillastrini 2009) and depends strongly on different impact parameters (Eneev et al. 1973). We find that  $R_{\text{vir}}$  of the Galaxy is  $\sim 250$  kpc and for M31 it is  $\sim 260$  kpc (Seigar et al. 2008; Majewski et al. 2007). Given that the distance between these two galaxies is  $\sim 780$  kpc (Ribas et al. 2005; McConnachie et al. 2005; Karachentsev & Kashibadze 2006), which is more than the double of the sum of their virial radii, we believe the tidal effect of M31 on overall mass estimate of the Galaxy, if any, should be negligible. The tidal effects of LMC and SMC on

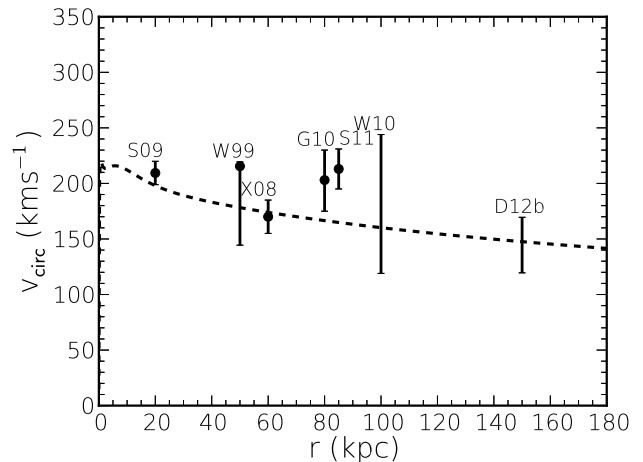


**Figure 11.** Dashed black line is our best fit model of  $v_{\text{circ}}$  given by red line in Figure 10. Black dots are the values from the literatures (Wilkinson & Evans 1999; Xue et al. 2008; Sofue et al. 2009; Watkins et al. 2010; Gnedin et al. 2010; Samurović & Lalović 2011; Deason et al. 2012b) labeled as W99, X08, S09, W10, G10, S11, and D12b respectively. To make the plot less obscure we do not include similar findings from the literature. For details about the similar results refer to the text.

the Galaxy have not been explored in this paper.

Note, our mass modeling of the Milky Way, does not make any assumption about the value of  $\beta$ , instead we use the value of  $\beta$  directly computed from the data. The only assumption that we make is that the density of the dark matter halo follows an NFW profile. As long as that assumption holds our estimates for  $v_{\text{circ}}$  and mass of the Milky Way should also be valid in the outer parts  $r > 25$  kpc where we cannot directly measure  $\beta$ . If one wants to directly measure  $v_{\text{circ}}$  in the outer parts using only line of sight velocities then one has to make an assumption about the underlying  $\beta$ . Several attempts have been made in this regard, with each of them making different assumptions about  $\beta$  and hence introducing a bias in the estimated mass. Below we compare these with our prediction for the mass of the Galaxy. Dashed line in Figure 11 is our best fit model of  $v_{\text{circ}}$ . Since literature sources mostly report mass within a certain radius, to facilitate comparison we convert it to  $v_{\text{circ}}$  using the relation

$$M(< r) = v_{\text{circ}}^2 r / G.$$

In Figure 11 the plotted  $v_{\text{circ}}$  from different sources span a wide range in radii and were computed using different types of tracer populations. By fitting a model to the kinematics of the satellite galaxies and the globular clusters, Wilkinson & Evans (1999) measure the mass to be  $M(50 \text{ kpc}) \sim 5.4_{-3.6}^{+0.2} \times 10^{11} M_{\odot}$ . This agrees with estimates by Kochanek (1996) ( $M(50 \text{ kpc}) = (4.9 \pm 1.1) \times 10^{11} M_{\odot}$ ) and Sakamoto et al. (2003) ( $M(50 \text{ kpc}) = 1.8 - 2.5 \times 10^{11} M_{\odot}$ ). Watkins et al. (2010) apply the tracer mass estimator formalism to 26 satellite galaxies and find that  $M(300 \text{ kpc}) = (0.9 \pm 0.3) \times 10^{12} M_{\odot}$ . Their mass estimate is however prone to the systematics introduced by assumed  $\beta$ , as duly mentioned by them. It can be seen in the figure that at  $r = 100$  kpc, depending upon the chosen anisotropy, their mass could vary anywhere between  $0.3 \times 10^{12} M_{\odot}$  and  $1.4 \times 10^{12} M_{\odot}$ . Studying the hyper-velocity stars within 80 kpc, and assuming  $\beta = 0.4$ , Gnedin et al. (2010) estimate  $M = 6.9_{-3.0}^{+1.2} \times 10^{11} M_{\odot}$ , which is slightly higher than our estimate. Using BHB stars and Watkins et al. (2010) tracer formalism Samurović & Lalović

<sup>2</sup> The disk model with  $b = 0$  is also otherwise known as Toomre's model or Kuzmin disk (Toomre 1963; Binney & Tremaine 2008)

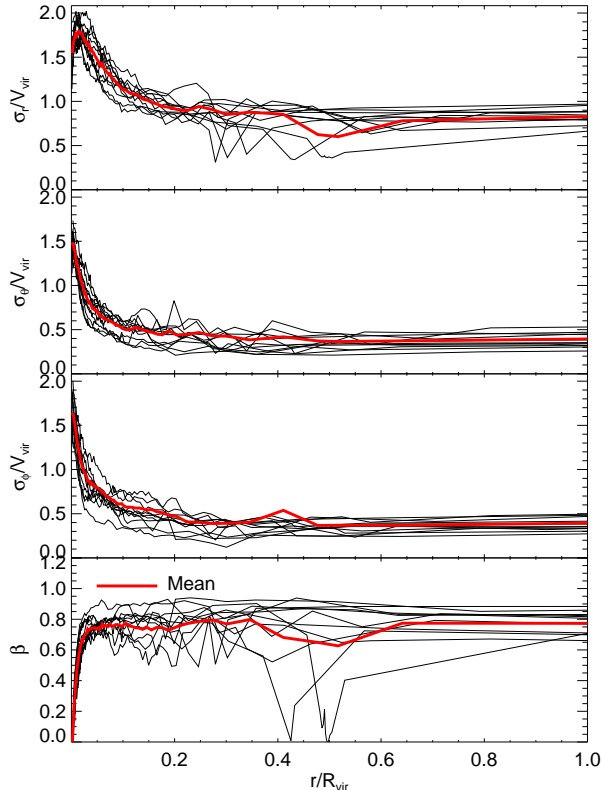


**Figure 12.** Velocity dispersions and anisotropy profiles of BHB stars in simulated stellar halo: From top to bottom are  $\sigma_r$ ,  $\sigma_\theta$ ,  $\sigma_\phi$ , and  $\beta$  profiles of the 11 instances of simulated halo taken from Bullock & Johnston (2005). The thick red lines are the mean profiles of the 11 halos.

(2011) estimate the mass at  $r = 85$  kpc to be  $8.83 \pm 0.73 \times 10^{11} M_\odot$ . This is slightly higher than our estimate, probably because they assume  $\beta = 0$ . With the mixed sample of tracers (BHB and CN stars) populating the outer-most halo ( $r \sim 50 - 150$  kpc), Deason et al. (2012b) estimated mass of the Galaxy to be  $M(150 \text{ kpc}) = (5 - 10) \times 10^{11} M_\odot$ . The variation is mainly due to uncertainty on the adopted potential and density slopes, and anisotropy. Their range of mass at the outer-most halo falls within our estimation.

## 6. KINEMATICS OF THE SIMULATED STELLAR HALO

We now study the kinematic properties of simulated stellar halos in which the halos are formed purely by accretion of satellite galaxies. For this we use the simulations of Bullock & Johnston (2005). In order to construct a synthetic sample of BHB stars from these simulations we use the code GALAXIA (Sharma et al. 2011a). Figure 12 shows the velocity dispersion and anisotropy profiles of 11 different  $\Lambda$ CDM halos as a function of galactocentric radius  $r$ . The mean of all the halos is also shown alongside as thick red line. In general the velocity dispersions fall off with radius. At small  $r$  the fall is rapid but at large  $r$  it is much slower. Asymptotically the ratio  $\sigma_r/V_{vir}$  approaches a value of around 0.8. The  $\beta$  rises rapidly from a value of zero in the center to about 0.8 at  $r \sim 10$  kpc, and thereafter shows very little change. These results are in good agreement with results of Abadi et al. (2006); Sales et al. (2007), who study the stellar halo formed in cosmological hydro-dynamical simulations including star formation and feedback.

Firstly notice that  $\Lambda$ CDM halos are rarely tangential for any

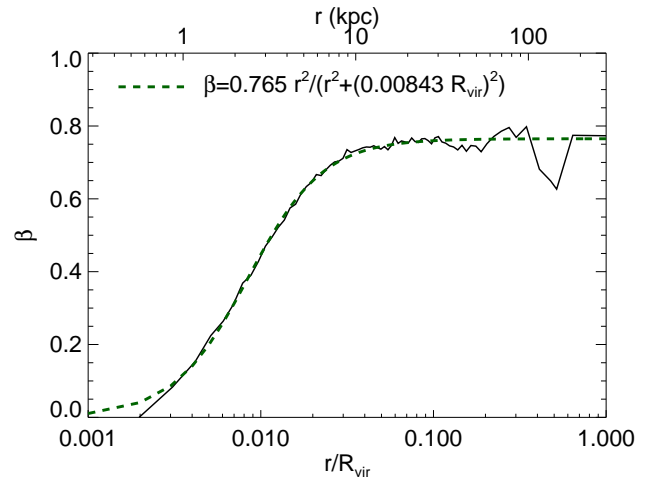


**Figure 13.** The mean  $\beta$  profile of BHB stars in 11 simulated  $\Lambda$ CDM stellar halos of Bullock & Johnston (2005). Shown alongside as dashed line is the best fit analytic function of form given by Cuddeford (1991).

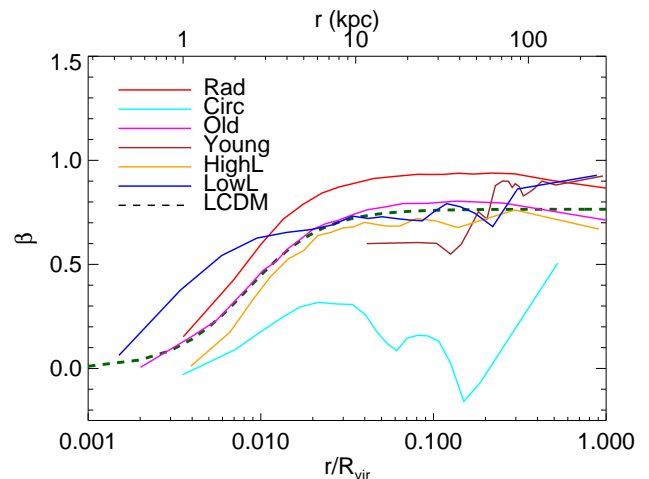


**Figure 14.** The  $\beta$  profile of simulated stellar halos having non-standard accretion history.

given radius. For most of the range of  $r$ ,  $\beta$  is in general greater than 0.5. We fit an analytic function of Cuddeford (1991) form given by

$$\beta(r) = \beta_0 \frac{r^2}{r^2 + r_0^2} \quad (16)$$

to the mean  $\beta$  profile of the 11  $\Lambda$ CDM halos. The best fit values of the free parameters were found to be  $\beta_0 = 0.765$  and  $r_0 = 0.00843 R_{vir}$ . Figure 13 shows that the fit is quite good for a wide range of  $r$ . The slight mismatch at  $r < 1$  kpc could be due to issues related to force resolution. In the outer parts most of the mass is in bound structures and hence is not smoothly distributed. This is probably responsible for the non-smooth behavior in  $\beta$  in the outer parts.

Figure 14 presents the beta profiles for halos having non- $\Lambda$ CDM accretion history, i.e., halos having accretion history significantly different from that predicted by the  $\Lambda$ CDM model of galaxy formation. Six halos that we consider are with accretion events being dominated by 1) radial orbits 2) circular orbits 3) old events 4) recent events 5) higher luminosity and 6) low luminosity and these are from simulations of Johnston et al. (2008). Signatures of different accretion events can be seen in the  $\beta$  profiles. The most significant dif-

ference is between the radial and the circular halo, which is expected since the orbital properties of the satellites were different to begin with. It is interesting to note that the circular halo is the only one among all the simulated halos that can have  $\beta < 0$ . The old halo almost perfectly follows the mean profile that we had derived for the 11  $\Lambda$ CDM halos and has the smoothest profile. This is due to the fact that the stars in this halo are completely phase mixed and have no structures of any kind. The young halo has very few stars in inner regions and shows non smooth behavior due to presence of significant amount of structures. The high luminosity halo is also very similar to old halo. However, the low-luminosity halo has higher  $\beta$  for  $r < 0.01R_{\text{vir}}$ . This is most likely due to circularization of orbits when acted upon by dynamical friction. Orbit circularization has also been reported by Sales et al. (2007) in their simulations. Note, the effect of dynamical friction is strongest for high luminosity events and weakest for low luminosity events. Moreover, satellites when acted upon by dynamical friction loose energy and move towards the inner regions of the halo. This partly explains as to why the high luminosity halo has low  $\beta$  in the inner regions as compared to the low luminosity halo.

In §3.2 we measured  $\beta$  until  $r = 23$  kpc. Beyond this we can measure  $\sigma_r$  out to  $r = 56$  kpc, but not  $\sigma_\phi$  and  $\sigma_\theta$ . By using the circular velocity curve that we derived in §5 we can predict  $\beta$  beyond  $r > 23$  kpc making use of the Jeans equation (Equation 7). To proceed we need to make an assumption about the density slope ( $\alpha$ ); beyond  $r > 27$  kpc it has been shown that  $\alpha$  is around 4.5. Assuming this, the predicted  $\beta$  is plotted in Figure 15. It can be seen that there is a slight jump in the value of  $\beta$  passing from  $r = 23$  kpc to  $r = 27$  kpc and beyond this the value of  $\beta$  is around 0.4. The sudden jump in  $\beta$  occurs via the Jeans equation (Equation 7), due to the discontinuity in  $\alpha$  ( $= -d\ln\rho/d\ln r$ ). Note, an assumption of steeper density slope would increase the  $\beta$  and vice versa. The red line in figure is the anisotropy profile fitted to the simulated  $\Lambda$ CDM halos given by Equation (16) from §6. It can be seen that accretion based models cannot explain the dip that is in observations, specially the profile in the region  $12 < r/\text{kpc} < 23$ . However, outside this region the simulations are roughly in agreement with observations. For  $r < 12$  kpc the observations match the value of around  $\beta = 0.5$  seen in simulations. For  $r > 23$  kpc the overall value of  $\beta$  in observations is slightly low but the profile is flat as in simulations. The outer halo at  $r = 56$  kpc is radial with  $\beta = 0.55$ .

## 7. CONCLUSION AND DISCUSSION

We study the kinematics of  $\sim 4500$  BHB stars to obtain the velocity dispersion profiles along three orthogonal axes in spherical polar coordinates using the gaussian velocity ellipsoidal (GVE) DF. GVE as an estimator of the velocity dispersion has the advantage that no assumptions about potential or density are needed *a priori*. From the estimated velocity dispersion profiles using maximum likelihood analysis, we also derive the anisotropy profile of the Galactic halo and compare it to the simulated  $\Lambda$ CDM halos. Finally, using radial velocity dispersion profile, anisotropy profile and density power law we constrain the mass of the Milky Way Galaxy using the Jeans equation.

We measure the  $\sigma_r$  profile of the halo out to  $r \sim 60$  kpc. At large distance ( $d \gg R_\odot$ ),  $\sigma_r$  can be approximated by  $\sigma_{\text{los}}$ . Thus in outskirts,  $\sigma_{\text{los}}$  profile given by Xue et al. (2008) converges to our  $\sigma_r$  profile. At  $r \sim 60$  kpc  $\sigma_r$  attains  $\simeq 100 \text{ km s}^{-1}$ . However, in the inner halo the approximation ( $\sigma_r \approx \sigma_{\text{los}}$ ) is

invalid and we find that the deviation of  $\sigma_{\text{los}}$  from  $\sigma_r$  is as high as  $\sim 40 \text{ km s}^{-1}$ . We obtain a  $\sigma_r(r)$  profile with plateau in the inner halo, a sudden fall at  $r \sim 15$  kpc and a gradual decline outwards. Qualitatively, similar profile is also found by Sommer-Larsen et al. (1997). However, our  $\sigma_r$  profile sharply falls at  $r \sim 15$  kpc whereas they find a gentle transition. The is probably due to the fact that they make an assumption that  $v_{\text{circ}}(r)$  is constant which we find is not completely true.

Next we estimate the tangential velocity dispersions,  $\sigma_\theta$  and  $\sigma_\phi$ . Using these estimates we are able to measure the  $\beta(r)$  till  $r = 25$  kpc. Astonishingly, we discover a dip in the  $\beta$  profile at  $r = 17$  kpc, where  $\beta \simeq -1.2$ . We find that the inner halo ( $r < 12$  kpc) is radial with  $\beta \simeq 0.5$ . This result of radially biased inner halo concurs with the recent results by Smith et al. 2009b; Bond et al. 2010 using the proper motions. Beyond the switch over point in the range  $18 \lesssim r/\text{kpc} \lesssim 25$  the anisotropy rises slightly and becomes isotropic to mild radial. We also verify the result using an alternative DF, namely the D11 DF. A small systematic in the  $\beta(r)$  profiles is seen from these two models which is mainly due to the assumption about density slope ( $\alpha$ ) that needs to be made *a priori* for D11 DF. We check for the contribution of the halo substructures, namely Virgo Overdensity and Sagittarius stellar stream, and find that they have little effect in the anisotropy profile. The effects of  $v_{\text{LSR}}$  and  $R_\odot$  upon our velocity dispersions and anisotropy estimates are also found to be negligible.

D11 study the BHB stars in the radial bin ( $10 < r/\text{kpc} < 25$ ) and find the halo to be tangential. After re-analyzing the D11 sample in this bin, we find that this is mainly because of the choice of their bin size that encompasses the transition region ( $13 < r/\text{kpc} < 17$ ) where we detected a dip in the  $\beta(r)$ . Possibly it could be also because of the degeneracy between potential and anisotropy in their model. However, in their recent work D12 break the degeneracy among their model parameters and measure  $\beta = 0.4^{+0.15}_{-0.2}$  with  $\alpha = 4.6$  in the region  $16 \lesssim r/\text{kpc} \lesssim 48$ . Within the range of uncertainty our value for  $\beta$  ( $-0.14^{+0.52}_{-0.66}$ ) using GVE model agrees with them. We find that D12 value of  $\beta \approx 0.4$  in this bin, although derive from a sample which is dominated by stars within  $r < 27$  kpc, is not appropriate for the range  $18 < r/\text{kpc} < 23$ , instead it is appropriate for the range  $23 < r/\text{kpc} < 48$ . Finally, we check how well we can estimate the mass and anisotropy together using D11 DF in the outer-most region ( $35 < r/\text{kpc} < 84$ ) We find that due to the lack of tangential information, a degeneracy between mass-anisotropy cannot be broken.

Substituting the estimates of  $\sigma_r(r)$  and  $\beta(r)$  in the Jeans equation, we then calculate the circular velocity profile of the Galaxy ( $v_{\text{circ}}(r)$ ). We detect the dip in the  $v_{\text{circ}}$  profile at 10-12 kpc, also seen by Sofue et al. (2009) at 9 kpc, which is attributed to the massless ring as a perturbation to the disk. Finally, we fit the three component (exponential disk, Hernquist bulge, and NFW halo) galaxy model to the observed  $v_{\text{circ}}$  profile in order to obtain the mass distribution of the Galaxy. From our best fit model, we calculate  $M_{\text{vir}}$  of the halo to be  $0.9^{+0.4}_{-0.3} \times 10^{12} M_\odot$  with  $R_{\text{vir}} = 249^{+34}_{-31}$  kpc and concentration parameter,  $c = 12.0^{+0.6}_{-0.5}$ . The mass of the Galaxy, within the extent we are able to constrain all the three components of velocity dispersions, is estimated to be  $M(r \lesssim 25 \text{ kpc}) = 2.1 \times 10^{11} M_\odot$ . Our estimate for  $M_{\text{vir}}$  is in good agreement with the most of the recent estimates namely by Watkins et al. (2010); Kochanek (1996); Wilkinson & Evans (1999); Sakamoto et al. (2003); Sofue et al. (2009); Watkins et al. (2010); Deason et al.

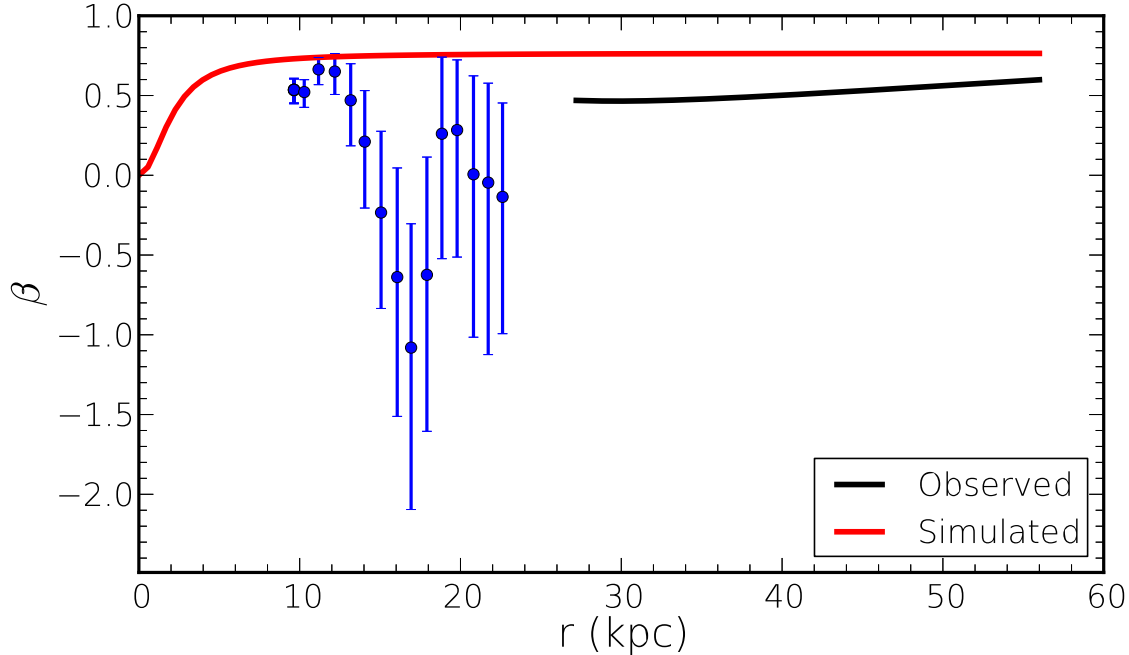


**Figure 15.** Black solid line is the observed  $\beta$  profile in the outer halo (assumed  $\alpha = 4.5$ ) whereas the red solid line is the  $\beta$  profile of the simulated halo. The blue dots with error bars are the observed values of  $\beta$  from section 3. The sudden jump in  $\beta$  profile passing from  $r = 23$  kpc to  $r = 27$  kpc could be a spurious effect due to our assumption of the broken power law with break at  $r = 27$  kpc.

(2012b) as demonstrated in Figure 11. In their studies of same population of stars (BHB), Xue et al. (2008) also fit a three component galaxy model and calculates  $M_{\text{vir}}$  to be  $0.91_{-0.18}^{+0.27} \times 10^{12} M_{\odot}$ . Our result for  $M_{\text{vir}}$  is in very good agreement with their estimate but our uncertainty is slightly larger. Note that they make an assumption about the  $(v_{\text{circ}}/v_{\text{los}})$  with radius from the simulations whereas we do not make any such assumption. Additionally, we also consider a more realistic three-dimensional disk model which is found to predict slightly higher Galactic mass  $M_{\text{vir}} = 1.2_{-0.4}^{+0.5} \times 10^{12} M_{\odot}$  with  $R_{\text{vir}} = 274_{-30}^{+35}$  kpc for flattening constant  $a = 2.5$ .

In the end, we used the measured quantities  $\sigma_r$  and  $v_{\text{circ}}$  to extend the  $\beta$  profile beyond  $r \sim 25$  kpc up to the distance where  $\sigma_r(r)$  can be confidently measured ( $r \sim 60$  kpc). The only assumption that we make here is about the density profile which we choose to be  $\alpha = 4.5$  in consent to the recent results by Watkins et al. (2009); Deason et al. (2011b). We find that the outer halo is radial and attains  $\beta = 0.55$  at  $r \sim 60$  kpc.

We also compare our result with simulated stellar halo which are formed purely by accretion (Bullock & Johnston 2005). This simulated halo is found to be in rough agreement to the observed halo in the inner region  $r < 12$  kpc. It is seen that in none of the instances of simulations the  $\beta$  profiles obtained could predict tangential halo at any distance and thus fails to explain a dip seen at  $r = 17$  kpc in observed  $\beta$  profile. In contrast, in the outer region ( $r > 25$  kpc) simulations and observations both agree in overall sense of the anisotropy and predict a flat anisotropy profile.

In all the observed quantities  $\sigma_r, \sigma_{\theta}, \sigma_{\phi}$  and  $\beta$  we see a dramatic shift in properties at  $r \sim 17$  kpc. We noticed that these undulations in the profiles are translated into our  $v_{\text{circ}}$  estimation resulting a varying  $v_{\text{circ}}$  profile. It could be true other way around, in a sense that the non-monotonic trends seen in all of our kinematic profiles could be due to the presence of so far unaccounted features in the Milky Way potential.

Alternatively, the shift in the properties seen in the observed profiles could possibly be an indication of a complex multi-component halo. Recently there have been series of works advocating multi-component halo. The studies of the calibration stars by Carollo et al. (2007) and Carollo et al. (2010) from the SDSS survey and the follow-up studies by Beers et al. (2012) have shown that the halo has at-least two distinct components. They associated the inner-halo to be formed in-situ whereas the outer halo are considered to be formed by accretion. Carollo et al. (2010) and de Jong et al. (2010) have found that the population fraction inversion point between the inner and outer halo lies between  $\sim 15 - 20$  kpc. Kinman et al. (2012) studied the BHB and RR Lyrae stars towards the galactic-anticenter and North Galactic Pole and found that the retrograde component of the halo dominates for  $r > 12.5$  kpc. It seems that this transition between the inner to the outer halo is recorded in the  $\beta$  of the halo as well. Additionally, duality in the formation history of the halo has also been seen in the recent smooth particle hydrodynamics and N-body simulations by Zolotov et al. (2009); McCarthy et al. (2012); Font et al. (2011). Kalirai (2012) recently attribute the age difference of 2 billion years in the halo components to in-situ and accretion. On the contrary, Schönrich et al. (2011) reanalyzed the calibration stars from Carollo et al. (2010) and find no reliable evidence of the existence of outer retrograde halo.

In a nutshell, the stellar halo is a test bed to understand the formation history of the galaxy. Even in this era where we have access to huge volume of spectroscopic and photometric data, the crucial physical quantities like velocity dispersions and anisotropy are not completely understood due to the lack of proper motions. With the advent of data inflowing in the coming decades through the magnificent next generation of spectroscopic survey like LEGUE (Deng et al. 2012) and specially, unprecedented proper motions from an astrometric mission like GAIA (Perryman 2002) will help to put strong

constrains on these fundamental quantities. Additionally, to see a bigger picture, confirming the results with the different stellar types or an alternative tracers is also crucial. Moreover, exploring the southern sky is equally important to complete the picture, for which up-coming spectroscopic survey like GALAH<sup>3</sup> will also play an important role.

#### ACKNOWLEDGEMENT

We sincerely thank the anonymous referee for comments those helped to improve the paper. We also thank Dr. Ralph Schonrich and Francesco Fermani for their comments on the manuscript, particularly on the effect of  $(v_{\text{LSR}}, R_{\odot})$ . Dr. Xiang Xiang Xue is thanked for the on-line publication of the clean sample of BHB stars. Mr. Tim White is also thanked

for the comments on original manuscript. PRK acknowledges University of Sydney International Scholarship (USydlS) for the support of his candidature. GFL acknowledges support from ARC Discovery Project DP0665574. J.B.H. is funded through a Federation Fellowship from the Australian Research Council (ARC) and S.S. is funded through ARC DP grant 0988751 which supports the HERMES project.

Funding for the SDSS and SDSS-II has been provided by the Alfred P. Sloan Foundation, the Participating Institutions, the National Science Foundation, the U.S. Department of Energy, the National Aeronautics and Space Administration, the Japanese Monbukagakusho, the Max Planck Society, and the Higher Education Funding Council for England. The SDSS Web Site is <http://www.sdss.org/>.

#### APPENDIX

##### A. BINNING AND EFFECT OF THE BIN SIZE

Here we investigate an effect of  $n_{\text{bin}}$  to our analysis. Figure 16 shows the velocity dispersion profiles and the anisotropy profile for the same sample of stars but with different particles in each bin. We see that with the decrease in the number of stars in each bin the uncertainties in the result increases. But the overall trend remains unaltered.

##### B. EFFECT OF $v_{\text{LSR}}$ AND $R_{\odot}$

In literatures there are varied claims about the value of  $v_{\text{LSR}}$  ranging from 184–270  $\text{kms}^{-1}$  (Olling & Merrifield 1998; Méndez et al. 1999; Reid et al. 2009; Bovy et al. 2009; Koposov et al. 2010). Similarly, the value of  $R_{\odot}$  is also disputable within 8–8.5 kpc (Reid 1993; Ghez et al. 2008; Gillessen et al. 2009). McMillan & Binney (2010) found that the ratio  $v_{\text{LSR}}/R_{\odot}$  can be better constrained than each of them alone and should range between 29.9–31.6  $\text{kms}^{-1}\text{kpc}^{-1}$ . Distressingly, there is still no consensus upon the values of  $(v_{\text{LSR}}, R_{\odot})$ . To study the effect of chosen values of  $(v_{\text{LSR}}, R_{\odot})$  upon our estimates of dispersion profiles we repeat the same analysis done to obtain the black diamond points in §3 (Figure 3). In Figure 17 we show the results for different values of  $(v_{\text{LSR}}, R_{\odot})$ . Here again the black diamond markers are obtained for a case  $(v_{\text{LSR}}, R_{\odot}) = (220.0 \text{ kms}^{-1}, 8.5 \text{ kpc})$  and is thus a replica of diamond points from Figure 3 put again for the ease of comparison. The red and black markers in the figure show the effect of chosen  $R_{\odot}$  values upon our estimates whereas the red, blue and cyan markers demonstrate the effect of chosen  $v_{\text{LSR}}$ . Within the range of  $(v_{\text{LSR}}, R_{\odot})$  investigated, the figure clearly demonstrates a negligible effect of them upon our estimates, given the range of uncertainties.

<sup>3</sup> <http://www.aao.gov.au/HERMES/GALAH/Home.html>

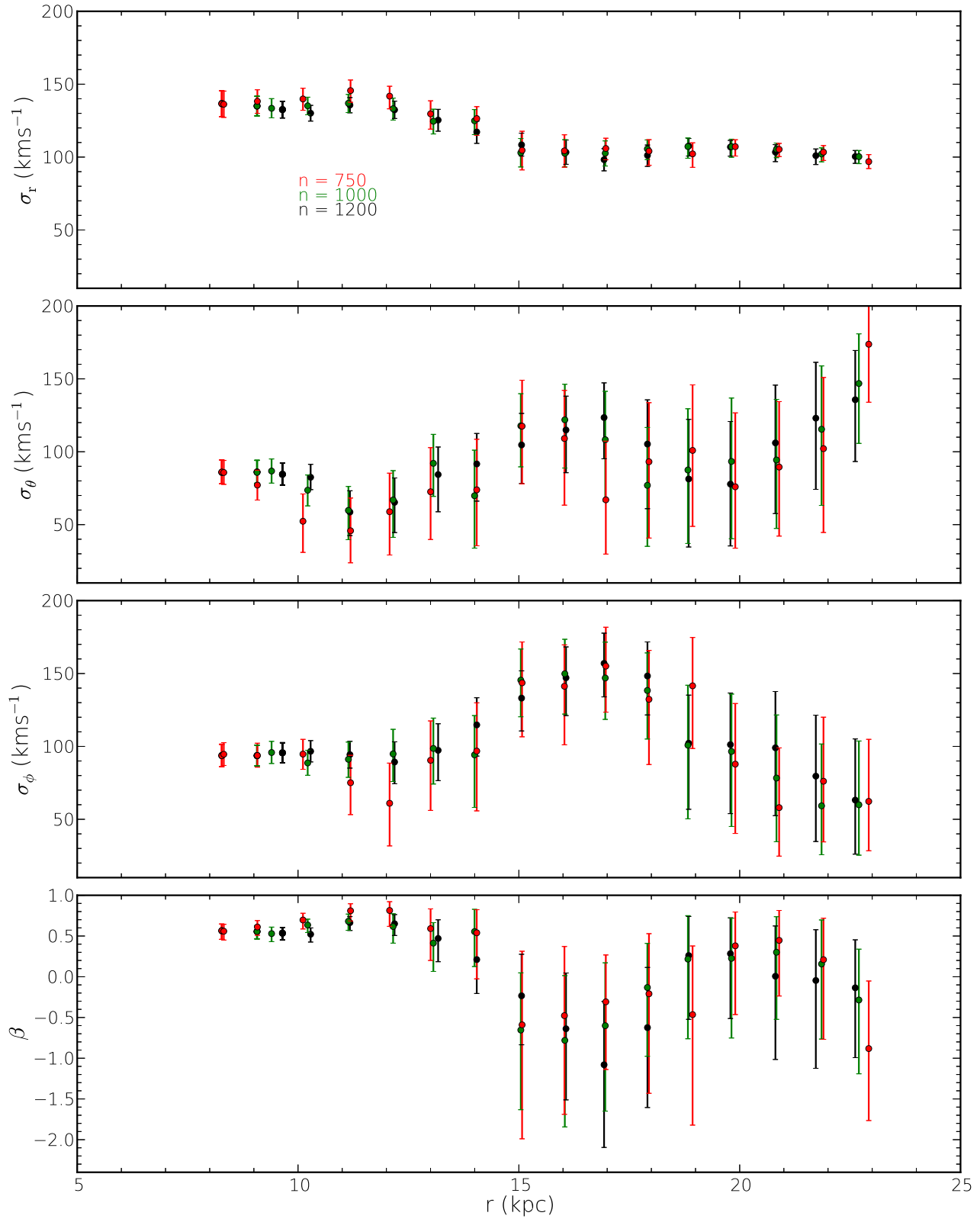


**Figure 16.** Effect of the number of particles in each CME bin. Red, green and blue points are the estimates with 750, 1000 and 1200 number of stars in each bin respectively. From top to bottom are the  $\sigma_r$ ,  $\sigma_\theta$ ,  $\sigma_\phi$  and anisotropy profile.



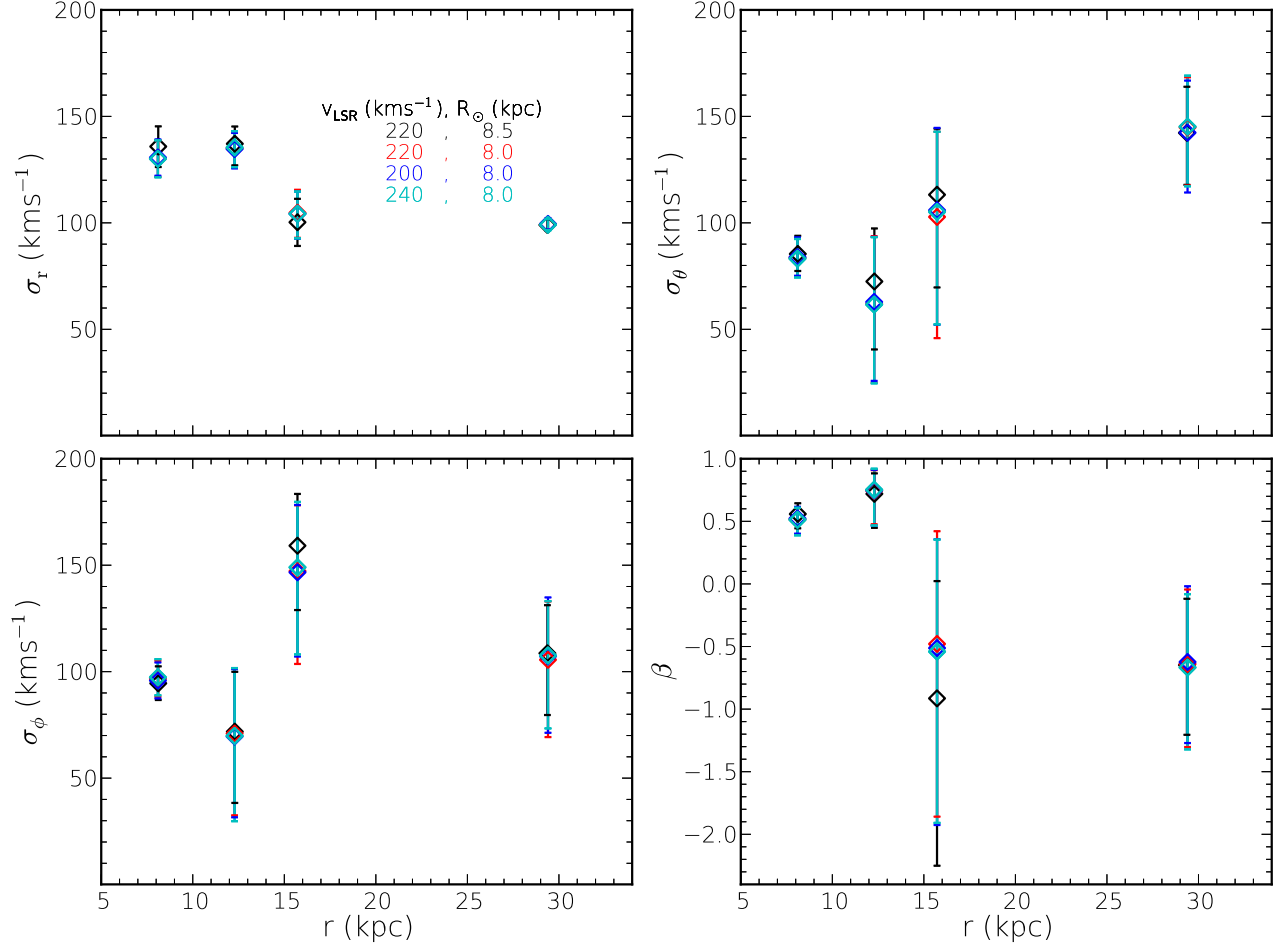


**Figure 17.** Velocity dispersion and anisotropy profiles for different combinations of  $v_{\text{LSR}}$  and  $R_{\odot}$ .

#### REFERENCES

- Abadi, M. G., Navarro, J. F., & Steinmetz, M. 2006, *MNRAS*, 365, 747  
 Abazajian, K. N., Adelman-McCarthy, J. K., Agüeros, M. A., et al. 2009, *ApJS*, 182, 543  
 Aihara, H., Allende Prieto, C., An, D., et al. 2011, *ApJS*, 193, 29  
 Baes, M., & Dejonghe, H. 2002, *A&A*, 393, 485  
 Baes, M., & van Hese, E. 2007, *A&A*, 471, 419  
 Baiesi Pillastrini, G. C. 2009, *MNRAS*, 397, 1990  
 Battaglia, G., Helmi, A., Morrison, H., et al. 2005, *MNRAS*, 364, 433  
 Beers, T. C., Carollo, D., Ivezić, Ž., et al. 2012, *ApJ*, 746, 34  
 Bell, E. F., Zucker, D. B., Belokurov, V., et al. 2008, *ApJ*, 680, 295  
 Belokurov, V., Zucker, D. B., Evans, N. W., et al. 2006, *ApJ*, 642, L137  
 Besla, G., Kallivayalil, N., Hernquist, L., et al. 2007, *ApJ*, 668, 949  
 Binney, J., & Tremaine, S. 2008, *Galactic Dynamics: Second Edition* (Princeton University Press)  
 Bland-Hawthorn, J. 2009, in *IAU Symposium, Vol. 254, IAU Symposium*, ed. J. Andersen, J. Bland-Hawthorn, & B. Nordström, 241–254  
 Blitz, L., Fich, M., & Stark, A. A. 1982, *ApJS*, 49, 183  
 Bond, N. A., Ivezić, Ž., Sesar, B., et al. 2010, *ApJ*, 716, 1  
 Bovy, J., Hogg, D. W., & Rix, H.-W. 2009, *ApJ*, 704, 1704  
 Brown, W. R., Geller, M. J., Kenyon, S. J., & Diaferio, A. 2010, *AJ*, 139, 59  
 Bryan, G. L., & Norman, M. L. 1998, *ApJ*, 495, 80  
 Bullock, J. S., & Johnston, K. V. 2005, *ApJ*, 635, 931  
 Burton, W. B., & Gordon, M. A. 1978, *A&A*, 63, 7  
 Carollo, D., Beers, T. C., Lee, Y. S., et al. 2007, *Nature*, 450, 1020  
 Carollo, D., Beers, T. C., Chiba, M., et al. 2010, *ApJ*, 712, 692  
 Clemens, D. P. 1985, *ApJ*, 295, 422  
 Cuadeford, P. 1991, *MNRAS*, 253, 414  
 de Jong, J. T. A., Yanny, B., Rix, H.-W., et al. 2010, *ApJ*, 714, 663  
 De Propriis, R., Harrison, C. D., & Mares, P. J. 2010, *ApJ*, 719, 1582  
 Deason, A. J., Belokurov, V., & Evans, N. W. 2011a, *MNRAS*, 411, 1480  
 —. 2011b, *MNRAS*, 416, 2903  
 Deason, A. J., Belokurov, V., Evans, N. W., & An, J. 2012a, *MNRAS*, L469  
 Deason, A. J., Belokurov, V., Evans, N. W., et al. 2012b, *MNRAS*, 425, 2840

- Dehnen, W., McLaughlin, D. E., & Sachania, J. 2006, *MNRAS*, 369, 1688
- Demers, S., & Battinelli, P. 2007, *A&A*, 473, 143
- Deng, L.-C., Newberg, H. J., Liu, C., et al. 2012, *Research in Astronomy and Astrophysics*, 12, 735
- Eisenhauer, F., Genzel, R., Alexander, T., et al. 2005, *ApJ*, 628, 246
- Eneev, T. M., Kozlov, N. N., & Sunyaev, R. A. 1973, *A&A*, 22, 41
- Evans, N. W., Hafner, R. M., & de Zeeuw, P. T. 1997, *MNRAS*, 286, 315
- Fich, M., Blitz, L., & Stark, A. A. 1989, *ApJ*, 342, 272
- Font, A. S., Benson, A. J., Bower, R. G., et al. 2011, *MNRAS*, 417, 1260
- Freeman, K., & Bland-Hawthorn, J. 2002, *ARA&A*, 40, 487
- Freeman, K. C. 1970, *ApJ*, 160, 811
- Frenk, C. S., & White, S. D. M. 1980, *MNRAS*, 193, 295
- Gerhard, O. E. 1991, *MNRAS*, 250, 812
- Ghez, A. M., Salim, S., Weinberg, N. N., et al. 2008, *ApJ*, 689, 1044
- Gillessen, S., Eisenhauer, F., Trippe, S., et al. 2009, *ApJ*, 692, 1075
- Gnedin, O. Y., Brown, W. R., Geller, M. J., & Kenyon, S. J. 2010, *ApJ*, 720, L108
- Helmi, A. 2008, *A&A Rev.*, 15, 145
- Helmi, A., & White, S. D. M. 1999, *MNRAS*, 307, 495
- Henon, M. 1973, *A&A*, 24, 229
- Honma, M., & Sofue, Y. 1997a, *PASJ*, 49, 539
- . 1997b, *PASJ*, 49, 453
- Honma, M., Bushimata, T., Choi, Y. K., et al. 2007, *PASJ*, 59, 889
- Ibata, R. A., Gilmore, G., & Irwin, M. J. 1994, *Nature*, 370, 194
- . 1995, *MNRAS*, 277, 781
- Jeans, J. H. 1915, *MNRAS*, 76, 70
- Johnston, K. V., Bullock, J. S., Sharma, S., et al. 2008, *ApJ*, 689, 936
- Jurić, M., Ivezić, Ž., Brooks, A., et al. 2008, *ApJ*, 673, 864
- Kalirai, J. S. 2012, *Nature*, 486, 90
- Karachentsev, I. D., & Kashibadze, O. G. 2006, *Astrophysics*, 49, 3
- Kinman, T. D., Cacciari, C., Bragaglia, A., Buzzoni, A., & Spagna, A. 2007, *MNRAS*, 375, 1381
- Kinman, T. D., Cacciari, C., Bragaglia, A., Smart, R., & Spagna, A. 2012, *MNRAS*, 422, 2116
- Kochanek, C. S. 1996, *ApJ*, 457, 228
- Komatsu, E., Smith, K. M., Dunkley, J., et al. 2011, *ApJS*, 192, 18
- Koposov, S. E., Rix, H.-W., & Hogg, D. W. 2010, *ApJ*, 712, 260
- Li, Y.-S., & White, S. D. M. 2008, *MNRAS*, 384, 1459
- Lin, D. N. C., & Lynden-Bell, D. 1982, *MNRAS*, 198, 707
- Macciò, A. V., Dutton, A. A., van den Bosch, F. C., et al. 2007, *MNRAS*, 378, 55
- Majewski, S. R. 1993, *ARA&A*, 31, 575
- Majewski, S. R., Ostheimer, J. C., Rocha-Pinto, H. J., et al. 2004, *ApJ*, 615, 738
- Majewski, S. R., Skrutskie, M. F., Weinberg, M. D., & Ostheimer, J. C. 2003, *ApJ*, 599, 1082
- Majewski, S. R., Beaton, R. L., Patterson, R. J., et al. 2007, *ApJ*, 670, L9
- Martin, N. F., Ibata, R. A., & Irwin, M. 2007, *ApJ*, 668, L123
- McCarthy, I. G., Font, A. S., Crain, R. A., et al. 2012, *MNRAS*, 420, 2245
- McConnachie, A. W., Irwin, M. J., Ferguson, A. M. N., et al. 2005, *MNRAS*, 356, 979
- McMillan, P. J., & Binney, J. J. 2010, *MNRAS*, 402, 934
- Méndez, R. A., Platais, I., Girard, T. M., Kozhurina-Platais, V., & van Altena, W. F. 1999, *ApJ*, 524, L39
- Merritt, D. 1985a, *MNRAS*, 214, 25P
- . 1985b, *AJ*, 90, 1027
- Miyamoto, M., & Nagai, R. 1975, *PASJ*, 27, 533
- Navarro, J. F., Frenk, C. S., & White, S. D. M. 1996, *ApJ*, 462, 563
- Newberg, H. J., Yanny, B., Rockosi, C., et al. 2002, *ApJ*, 569, 245
- Olling, R. P., & Merrifield, M. R. 1998, *MNRAS*, 297, 943
- Osipkov, L. P. 1979, *Soviet Astronomy Letters*, 5, 42
- Perryman, M. A. C. 2002, *Ap&SS*, 280, 1
- Reid, M. J. 1993, *ARA&A*, 31, 345
- Reid, M. J., Menten, K. M., Zheng, X. W., et al. 2009, *ApJ*, 700, 137
- Ribas, I., Jordi, C., Vilardell, F., et al. 2005, *ApJ*, 635, L37
- Rocha-Pinto, H. J., Majewski, S. R., Skrutskie, M. F., Crane, J. D., & Patterson, R. J. 2004, *ApJ*, 615, 732
- Sakamoto, T., Chiba, M., & Beers, T. C. 2003, *A&A*, 397, 899
- Sales, L. V., Navarro, J. F., Abadi, M. G., & Steinmetz, M. 2007, *MNRAS*, 379, 1464
- Samurović, S., & Lalović, A. 2011, *A&A*, 531, A82
- Schödel, R., Ott, T., Genzel, R., et al. 2002, *Nature*, 419, 694
- Schönrich, R., Asplund, M., & Casagrande, L. 2011, *MNRAS*, 415, 3807
- Schönrich, R., Binney, J., & Dehnen, W. 2010, *MNRAS*, 403, 1829
- Searle, L., & Zinn, R. 1978, *ApJ*, 225, 357
- Seigar, M. S., Barth, A. J., & Bullock, J. S. 2008, *MNRAS*, 389, 1911
- Sharma, S., Bland-Hawthorn, J., Johnston, K. V., & Binney, J. 2011a, *ApJ*, 730, 3
- Sharma, S., Johnston, K. V., Majewski, S. R., Bullock, J., & Muñoz, R. R. 2011b, *ApJ*, 728, 106
- Sirko, E., Goodman, J., Knapp, G. R., et al. 2004a, *AJ*, 127, 899
- . 2004b, *AJ*, 127, 914
- Smith, M. C., Wyn Evans, N., & An, J. H. 2009a, *ApJ*, 698, 1110
- Smith, M. C., Ruchti, G. R., Helmi, A., et al. 2007, *MNRAS*, 379, 755
- Smith, M. C., Evans, N. W., Belokurov, V., et al. 2009b, *MNRAS*, 399, 1223
- Sofue, Y., Honma, M., & Omodaka, T. 2009, *PASJ*, 61, 227
- Sommer-Larsen, J., Beers, T. C., Flynn, C., Wilhelm, R., & Christensen, P. R. 1997, *ApJ*, 481, 775
- Toomre, A. 1963, *ApJ*, 138, 385
- Watkins, L. L., Evans, N. W., & An, J. H. 2010, *MNRAS*, 406, 264

- Watkins, L. L., Evans, N. W., Belokurov, V., et al. 2009, MNRAS, 398, 1757  
White, S. D. M., & Rees, M. J. 1978, MNRAS, 183, 341  
Wilkinson, M. I., & Evans, N. W. 1999, MNRAS, 310, 645  
Wolfire, M. G., McKee, C. F., Hollenbach, D., & Tielens, A. G. G. M. 1995, ApJ, 453, 673  
Xue, X. X., Rix, H. W., Zhao, G., et al. 2008, ApJ, 684, 1143  
Xue, X.-X., Rix, H.-W., Yanny, B., et al. 2011, ApJ, 738, 79  
Yanny, B., Rockosi, C., Newberg, H. J., et al. 2009, AJ, 137, 4377  
Zolotov, A., Willman, B., Brooks, A. M., et al. 2009, ApJ, 702, 1058